

Citation for published version:

Ginzburg, D, Pinto, F, Iervolino, O & Meo, M 2017, 'Damage tolerance of bio-inspired helicoidal composites under low velocity impact', *Composite Structures*, vol. 161, pp. 187-203. https://doi.org/10.1016/j.compstruct.2016.10.097

DOI

10.1016/j.compstruct.2016.10.097

Publication date: 2017

Document Version
Peer reviewed version

Link to publication

Publisher Rights CC BY-NC-ND

# **University of Bath**

## **Alternative formats**

If you require this document in an alternative format, please contact: openaccess@bath.ac.uk

**General rights** 

Copyright and moral rights for the publications made accessible in the public portal are retained by the authors and/or other copyright owners and it is a condition of accessing publications that users recognise and abide by the legal requirements associated with these rights.

Take down policy

If you believe that this document breaches copyright please contact us providing details, and we will remove access to the work immediately and investigate your claim.

Download date: 09. Mar. 2023

# Damage Tolerance of Bio-Inspired Helicoidal Composites under Low Velocity Impact

D. Ginzburg, F. Pinto, O. Iervolino, M. Meo\*

Material Research Centre, Department of Mechanical Engineering, University of Bath,

Bath, BA2 7AY, UK

\*Corresponding author: m.meo@bath.ac.uk

## **Abstract**

It is well known that laminated composite materials are prone to impact damage caused by foreign objects and exhibit poor damage resistance in through the thickness direction. By drawing inspiration from naturally occurring impact resistant structures, such as dactyl clubs of mantis shrimp, enhanced damage tolerance and impact energy absorption can be achieved with traditional CFRP layers by creatively arranging them into bio-inspired configurations, called helicoidal or Bouligand structures. Through an extensive numerical analyses of low velocity impact (LVI) supported by the experimental results, a further insight into the possibilities that these structures can offer in terms of damage resistance was attained. By comparing the results of three square plates with different planar sizes, it was shown that the helicoidal layups are more effective at absorbing energy while minimising through the thickness failure than standard quasi-isotropic and cross-ply laminates. Although the helicoidal composites generally exhibited a higher degree of delamination in LVI tests, the standard lamination schemes displayed higher degree of perforation, which resulted in a reduced residual strength in the compression after impact (CAI) testing of a quasi-isotropic laminate compared to several helicoidal ones subjected to 40 J and 80 J impact energy. Furthermore, using advanced finite element analysis (FEA) code LS-DYNA® for simulating LVI and CAI events, it was revealed that the helicoidal arrangement endured the least amount of fibre damage.

Keywords: helicoidal, twisted, low velocity impact, Bouligand, composite damage, LS-DYNA®, MAT162

#### 1. Introduction

In structural sense, natural materials are incredibly efficient, satisfying a wide range of often competing requirements such as strength and toughness, while utilising as little amount of material as possible. Practically, all natural materials are composites comprised of rather limited selection of constituents such as collagen, keratin and fibroin proteins [1]. Characteristic dimensions of these biostructures range from nanoscale to macroscale and they typically consist of hard and soft segments organized in complex hierarchical architectures and therefore have proven challenging to replicate synthetically [2].

It took hundreds of millions of years of convergent evolution for nature to create multifunctional dermal armour present in fish (e.g. Arapaima gigas and Coelacanth), reptiles (e.g. crocodilian and squamata), and mammals (e.g. armadillo and pangolin) [3]. It usually consists of hierarchical structures with collagen fibres linking rigid scales/osteoderms for enhanced flexibility while maintaining strength properties [4]. These structures serve a range of purposes such as body protection, thermal regulation, coloration for supressing intra-species recognition and decreasing hydrodynamic drag in fish, thereby making these materials multifunctional by nature [5]. The shapes and forms of these natural protection units vary but they all exhibit several common characteristics of relatively low density / light weight, high strength, capacity for energy absorption and conformance to the body shape in order to facilitate rapid motion and agility. For example, scales of fish are typically comprised of a combination of a rigid protective external layer and a flexible internal one providing mobility and effective load distribution [3].

Evidently, it is important to study these creatures with naturally occurring armour as it can lead to fabrication of synthetic structures mimicking the advanced mechanical architectures of their natural counterparts. One particularly interesting feature of naturally strong materials, which is a subject of this study, is a helicoidal arrangement present in several strong and damage-resisting creatures. Bouligand [6] studied the existence of twisted morphologies in various Crustaceans by observing the bow/arc-shaped fibrous patterns using electron and light microscopy. In close examination of these transverse cross-sections, Bouligand concluded that these periodic patterns are in fact formed by stacked laminae of aligned fibres with each layer rotated by a small angle relative to the previous one producing a twisted (helicoidal) arrangement - Figure 2.1 graphically demonstrates an example of twisted/helicoidal or also known as Bouligand architecture. A number of biological systems reveal a twisted laminated structure, however, one of the most remarkable ones incorporating such a configuration is mantis shrimp or stomatopods which is an ancient member of an order of crustaceans, Stomatopoda - Figure 1.1 schematically shows the mantis shrimp highlighting its biological hammer.

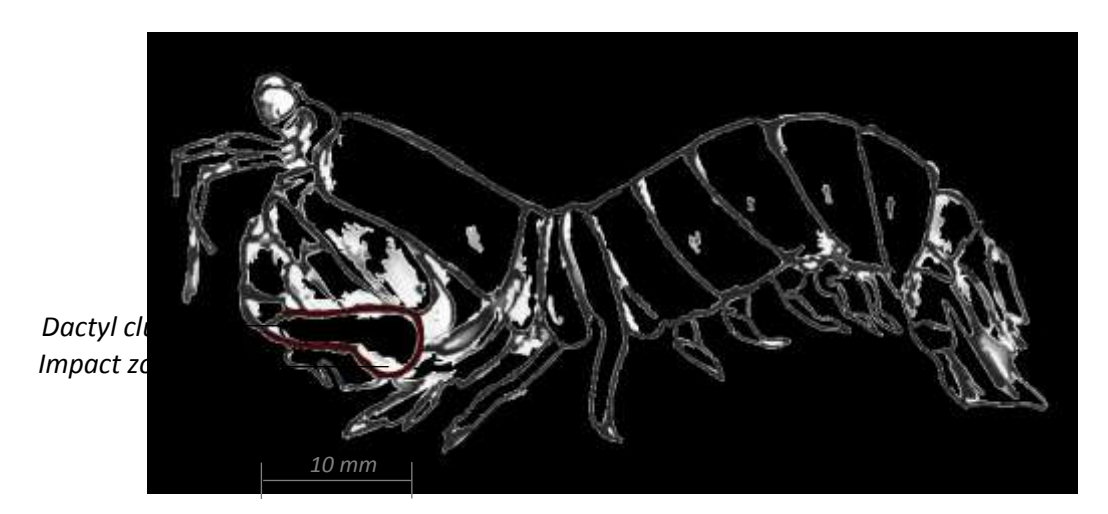


Figure 1.1: a sketch of an Odontodactylus scyllarus which is also known as peacock mantis shrimp.

Dactyl clubs of the stomatopods are adapted for withstanding many thousands of high velocity (over 20 m/s) impacts on sea shells and other prey on which they feed [7]. The micro and macro mechanical features of dactyl clubs reveal a range of impact-resisting characteristics not seen in other damagetolerant bio-composites such as shells [8, 9]. Hammer-like clubs of mantis shrimp have a virtually constant and well defined point of impact which has been biologically optimized for damage resistance [9]. They are formed of a multiphase composite incorporating oriented crystalline hydroxyapatite and amorphous calcium phosphate arranged into a highly expanded helicoidal organization containing fibrillar chitinous organic matrix; a structural combination of these elements acts as an effective line of defence preventing a catastrophic failure during repetitive high-energy loading events typically exceeding 200 N [8]. The club is comprised of a hard impact region (about 1 mm thick) exhibiting high Young's modulus and high strength, and a periodic (helicoidal) region (2-3 mm thick) of much lower and oscillating modulus of elasticity. In the periodic layer, chitin fibres are stacked forming a twisted configuration, whereby each layer has fibres oriented parallel to each other with each layer rotated to a certain pitch angle relative to the layer underneath resulting in a Bouligand structure [8]. Such a two phase organization is not exclusive to stomatopods. One of the largest freshwater fish, Arapaima gigas has scales with characteristic dimension of 50–100 mm which are composed of an external highly mineralized layer with ridges and an internal layer of collagen fibres in orientations describing a helicoid or Bouligand architecture [4]. This structure is also found in one the oldest and rarest surviving orders of fish, coelacanths [10]. Weaver et al. [8] explained that this hard-soft two phase organisation is effective in arresting the crack-propagation during impact - a crack approaching the impact surface encounters an elastic modulus mismatch which can either be deflected at the interface or propagated through the stiffer region [8].

There are many more examples of helicoidal structures present in nature such as the osteons in mammalian bones [11], certain plant cell walls, various insect cuticles [12] and DNA structure. Motivated by these examples, several authors have studied the applicability of these twisted laminae arrangements to conventional design of laminates using plates manufactured from various fibrereinforced composite pre-pregs [13-16]. In all the studies, unidirectional composite plates consisting of aligned fibre layers/plies mimicking those observed in the crustacean exoskeleton were fabricated and examined under a range of loading conditions. A helicoidal lamination sequence/layup is readily achieved by stacking of unidirectional layers with a gradual change in ply orientation from layer to layer. Changes in ply orientation are known to influence the toughness and strength of composite materials by altering damage mechanisms and damage propagation [17]. Motivated by Bouligand structure observed in beetle exoskeleton, Chen et al. [12] reported that fracture toughness of glass fibre-reinforced composites is significantly higher for helicoidal layups compared to that of a unidirectional control under static loading conditions. Apichattrabrut and Ravi-Chandar [13] performed tension, bending and high-velocity impact (HVI) tests along with linear finite element analysis (FEA) in an attempt to characterize an arbitrary helicoidal layup versus unidirectional and cross-ply laminates using carbon/epoxy pre-pregs. Helicoidal architecture showed improved debonding resistance and higher energy absorption facilitating penetration resistance in comparison to control layups. Most recently, Ngern et al. [16] reported on damage resistance of helicoidal compared to cross-ply composites comprised of carbon/epoxy material under ballistic impact loading. The results for the helicoidal configuration yielded higher ballistic limit for smaller inter-ply angle with larger delamination area providing a mechanism for energy absorption during impact loading. Inspired by the twisted architecture of the periodic phase observed in dactyl clubs of stomatopods, Grunenfelder et al. [15] explored several helicoidal layups featuring several inter-ply angle configurations against a quasi-isotropic laminate by means of experimental programme as well as nonlinear explicit FEA methods. Through low velocity impact (LVI) and compression after impact (CAI) testing, helicoidal composites retained higher residual strength compared to quasi-isotropic control samples [15]. Also, some interesting visualization of various damage modes obtained via numerical modelling of LVI was presented.

Past studies focused on comparing helicoidal layups against unidirectional, cross-ply and quasi-isotropic ones considering fibre-reinforced composite plates under static and dynamic loading. This study is an effort to expand that knowledge by examining the behaviour of twisted composite configurations arranged in plates of various width-to-thickness ratios. Cross-ply and quasi-isotropic layups were used as controls because both of these configurations are considered a standard in the aerospace industry especially in applications requiring damage-tolerance capabilities. Dynamic loading via LVI events with impact energies of 40J and 80J as well as CAI testing were used for the investigation. Experimental campaign reported herein was primarily carried out in order to validate an advanced FEA approach used for further analysis.

#### 2. Helicoidal Laminates

#### 2.1. Layup Consideration

The choice of the lamination sequence is crucial in defining a helicoidal laminate and effectively depends on the chosen angle difference between the adjacent plies referred to as pitch or rotation angle. Previous research efforts used pitch angles of 8° (48 plies [15], 24 plies [14]), 10° (40 plies [13]), 16° (48 plies [15], 24 plies [14]) and 26° (48 plies [15], 24 plies [14]). In the present work, in order to investigate how the different pitch angles affect the impact resistance of the laminate, two different angles were considered, namely 6° in layup LS3 and 12° in layups LS4 and LS5 – see Figure 2.1 and Table 2-1. It is important to underline that the choice of a specific pitch angle can affect the overall symmetry and balance of the laminate for a given total number of layers which would in turn affect the loading and deformation behaviour. For example, taking 32 plies and setting the pitch angle to 3° for the helicoidal arrangement, the plies in the stack would rotate from 0° to merely 93° resulting in an unsymmetrical and unbalanced layup which in turn would lead to certain generally undesired effects which are addressed later on in this section.

In order to achieve symmetry and/or balance of the helicoidal laminate, some researchers [13] added several additional mid-plane layers in the laminate sequence. In general, the larger the total number of layers the more flexibility a designer has in terms of the choice of the pitch angle and ultimately the lamination scheme. Guided by the previously published research, cost considerations and the manufacturing constraints, the total number of layers used in this study was fixed at 32 for each plate leading to an overall plate thickness of 4 mm. Figure 2.1 graphically displays the layup arrangements used in this work.

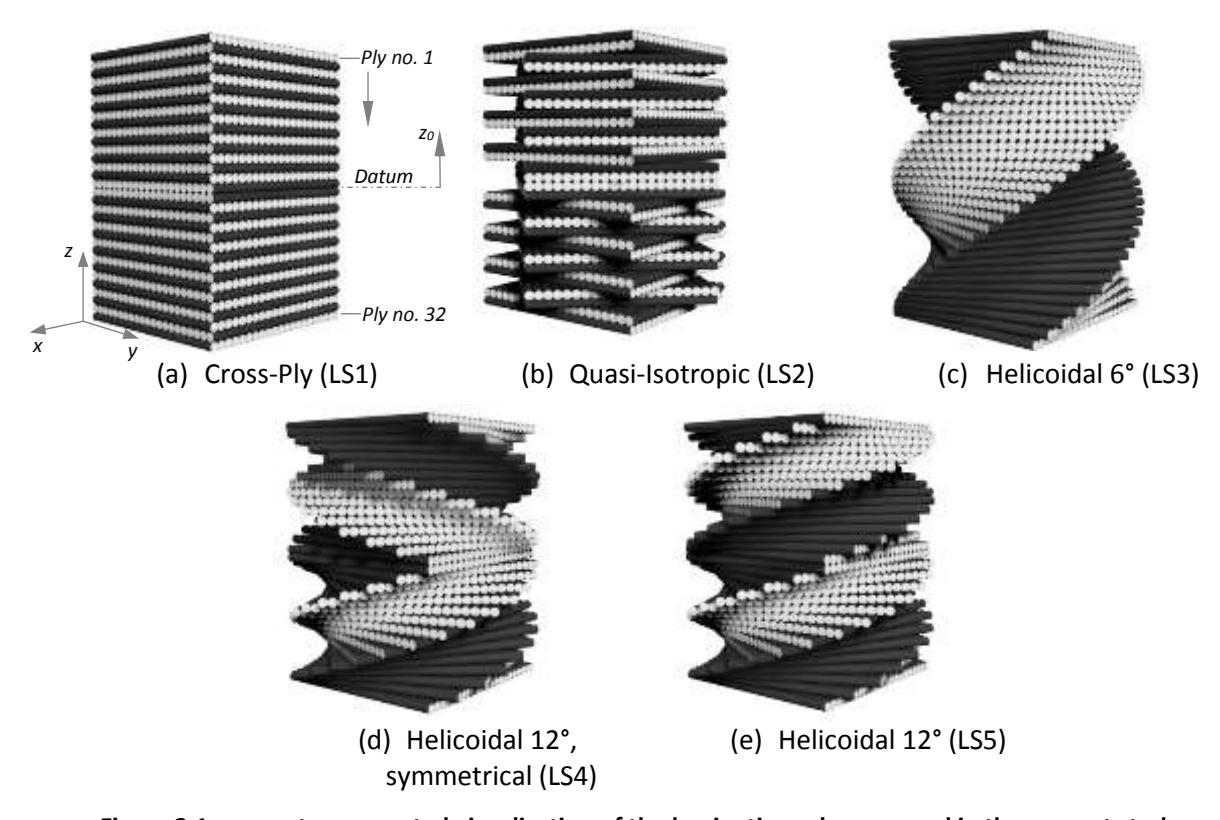


Figure 2.1: computer generated visualisation of the lamination schemes used in the present study.

Table 2-1 presents the specifications of the chosen layup configurations.

No.	No. of layers	Stacking Sequence	Туре	Description	Flatness After Curing
LS1	32	[0/90]8s	Cross-Ply	Symmetrical, balanced	Flat
LS2	32	[+45/-45/0/90]4s	Quasi-Isotropic	Symmetrical, balanced	Flat
LS3	32	[0/6/12/18//180]	Helicoidal (6°)	Non-Symmetrical, balanced	Induced twist
LS4	32	[0/12/24/36//180]s	Helicoidal (12°)	Symmetrical, balanced	Flat
LS5	32	[0/12/24/36//360]	Helicoidal (12°)	Non-Symmetrical, balanced	Induced twist

Table 2-1: specifications of the lamination sequences used in this study.

The non-symmetry of the stacking sequence combined with the directionally dependant coefficients of thermal expansion driven by the orthotropic nature of the composite plates leads to the physical twisting of the laminate, while net effect of the non-balance is to induce curvature. Curvature and twisting in laminated composite components are usually undesired and can physically occur during a typical curing process in an autoclave under elevated thermal conditions. This can be further examined by performing an analysis using classical laminated plate theory (CLPT) with nominal elastic properties of the CFRP plies used in the study (Table 2-2).

E <sub>11</sub> (GPa)	E <sub>22</sub> (GPa)	G <sub>12</sub> (GPa)	V <sub>xy</sub>	
160.5	12.5	4.6	0.303	

Table 2-2: mechanical properties of the CFRP used for CLPT analysis.

Matrices of extensional stiffness A (GPa  $\cdot$  mm), bending-extensional coupling stiffness B (GPa  $\cdot$  mm<sup>2</sup>)

and bending stiffness 
$$D$$
 (GPa · mm<sup>3</sup>) of the cross-ply (LS1) laminate are:
$$A = \begin{bmatrix} 348.5 & 15.3 & 0 \\ 15.3 & 348.5 & 0 \\ 0 & 0 & 18.4 \end{bmatrix}, B = 0, D = \begin{bmatrix} 501.9 & 20.4 & 0 \\ 20.4 & 427.4 & 0 \\ 0 & 0 & 24.5 \end{bmatrix};$$
(1)

the quasi-isotropic (LS2) laminate:

sotropic (LS2) laminate:  

$$A = \begin{bmatrix} 274.4 & 89.4 & 0 \\ 89.4 & 274.4 & 0 \\ 0 & 0 & 92.5 \end{bmatrix}, B = 0, D = \begin{bmatrix} 363.6 & 137.7 & 10.5 \\ 137.7 & 331.0 & 10.5 \\ 10.5 & 10.5 & 141.9 \end{bmatrix};$$
(2)

the helicoidal (LS3) laminate:

$$A = \begin{bmatrix} 279.0 & 84.7 & 0 \\ 84.7 & 279.0 & 0 \\ 0 & 0 & 87.9 \end{bmatrix}, B = \begin{bmatrix} 0 & 0 & -109.1 \\ 0 & 0 & -68.2 \\ -109.1 & -68.2 & 0 \end{bmatrix}, D = \begin{bmatrix} 635.2 & 97.9 & 0 \\ 97.9 & 139.0 & 0 \\ 0 & 0 & 102.1 \end{bmatrix};$$
(3)

the helicoidal (LS4) laminate

$$A = \begin{bmatrix} 297.7 & 84.7 & 0 \\ 84.7 & 260.4 & 0 \\ 0 & 0 & 87.9 \end{bmatrix}, B = 0, D = \begin{bmatrix} 463.4 & 107.2 & 101.7 \\ 107.2 & 292.3 & 62.7 \\ 101.7 & 62.7 & 111.4 \end{bmatrix};$$
(4)

the helicoidal (LS5) laminate:

$$A = \begin{bmatrix} 297.7 & 84.7 & 0 \\ 84.7 & 260.4 & 0 \\ 0 & 0 & 87.9 \end{bmatrix}, B = \begin{bmatrix} 0 & 0 & -50.8 \\ 0 & 0 & -31.3 \\ -50.8 & -31.3 & 0 \end{bmatrix}, D = \begin{bmatrix} 463.4 & 107.2 & 0 \\ 107.2 & 292.3 & 0 \\ 0 & 0 & 111.4 \end{bmatrix}.$$
 (5)

For a general kth layer of a laminate, the thermo-elastic stress-strain relationship can be calculated as [18]:

$$\{\sigma\}^{(k)} = [\mathbf{C}]^{(k)} (\{\varepsilon\}^{(k)} - \{\alpha_T\}^{(k)} \Delta T), \tag{6}$$

where  $\sigma$  and  $\varepsilon$  are stress and strain vectors in the laminate coordinate system respectively,  $\boldsymbol{C}$  is the stiffness matrix,  $\alpha_T$  is a vector of thermal expansion coefficients and  $\Delta T$  is a given temperature gradient. Applying the CLPT and Eq. (6) with a thermal gradient of 180°C representative of a typical curing cycle, the residual thermal stresses for each ply can be estimated as shown for the quasi-isotropic (LS2) and helicoidal (LS3) laminates in Figure 2.2 and in Figure 2.3 respectively.

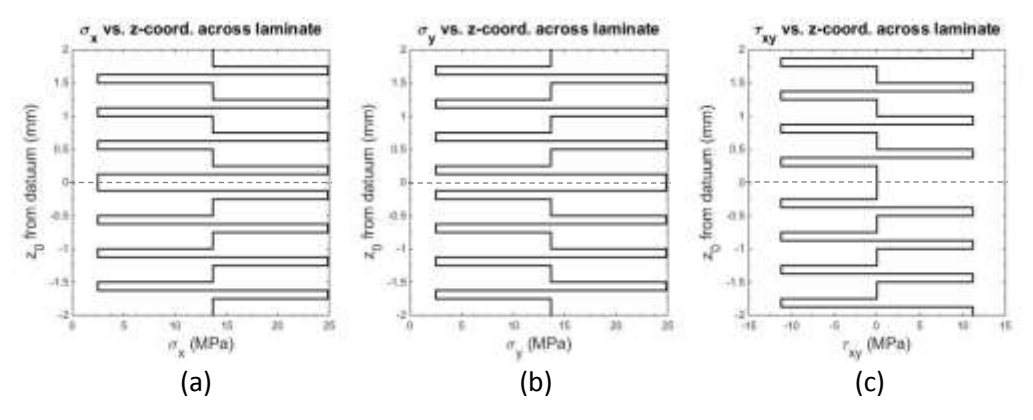


Figure 2.2: stress distributions in quasi-isotropic (LS2) laminate subjected to thermal gradient as predicted by CLPT.

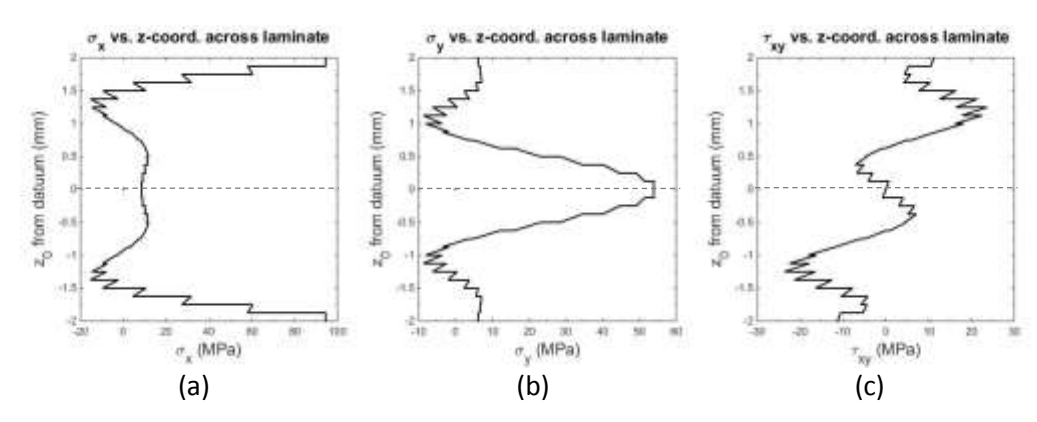


Figure 2.3: stress distributions in helicoidal (LS3) laminate subjected to thermal gradient as predicted by CLPT.

It can be clearly seen that both layups are balanced as normal principal stresses are symmetric about the mid-plane (datum) of the laminate which is further confirmed by the fact that the in-plane shear stiffnesses  $A_{16}$  and  $A_{26}$  of the extensional stiffness matrix are zero for all laminates. On the contrary, the through-thickness distribution of the in-plane shear stress  $\tau_{xy}$  of the helicoidal layup LS3 is non-symmetric about the datum plane - Figure 2.3. This in turn leads to the thermally induced twist of the laminate. Consequently, in order to avoid possible twist-induced shape inconsistencies of the plates, only the symmetric and balanced layups are considered in the experimental work which aimed at validating the numerical model. However, in the subsequent numerical analysis, the effect of the non-symmetry on the dynamic response and damage tolerance is studied considering a pitch angle of 12° in symmetric laminate LS4, which has the ply orientations mirror-imaged about its structural midplane, and LS5 which features the same pitch angle but the laminate is asymmetric. In fact, both LS3 and LS5 are characterised by the coupling between the in-plane and flexural behaviour (B matrix  $\neq$  0), whereas all laminates in this study are balanced and therefore do not exhibit coupling between the in-plane axial and shear deformations (since  $A_{16}$  and  $A_{26}$  = 0).

Previous studies indicated that helicoidal laminates can display better overall damage resistance by dissipating impact energy in-plane. Therefore, in this study, it is hypothesised that by increasing the planer size of the composite plates arranged using the helicoidal layups should provide an enhanced damage resistance (especially through the thickness) as there is a larger available area to distribute the impact energy. In order to evaluate how the increasing planar dimensions affect the response of helicoidal composites against the controls, three plate sizes, namely 100 mm x 100 mm, 200 mm x 200 and 300 mm x 300 mm were used. A square shape of the samples was chosen in order to avoid the directionality of the damage and fracture surfaces that can be associated with the aspect ratio. Although this is a deviation from the standard requirement of 150 mm x 100 mm, square geometry was used by a number of authors to study the impact response of composite plates for similar reasons [19, 20].

# 2.2. Experimental Setup

The primary purpose of the experimental work was to validate the numerical model so that further simulations could be performed without their experimental counterparts with a certain confidence level. Due to the fact the non-symmetrical layups LS3 and LS5 produce undesired twist during manufacturing, they were not considered during the physical testing in order to avoid inconsistencies induced by the possible variability of the shape across various samples. Only two plate dimensions with lamination schemes LS1, LS2 and LS3 were evaluated during the validation process, namely 100 mm x 100 mm and 200 mm x 200 mm. Four sets of identical test samples were manufactured and tested for each configuration (i.e. plate size, impact energy and layup) in order to assess the repeatability of results.

#### 2.2.1. Sample Manufacturing

A standard manual layup and vacuum bagging procedure was followed for manufacturing of the samples. The basic layer employed for the fabrication of the laminates in the work was a unidirectional carbon fibre epoxy prepreg T800/M21 (Hexcel®). All prepreg plies were cut to specific angles prior to laying up procedure. The temperature and pressure cycle used in the autoclave for curing the specimens was according to the manufacturer's material data sheet. After curing, the composite samples were machined to square dimensions of 120 mm x 120 mm and 220 mm x 220 mm using a water-fed diamond saw. A clearance of 20 mm was added to the plates in order to enable appropriate clamping during the subsequent testing, where the exposed part of the plates measured 100 mm x 100 mm and 200 mm x 200 mm.

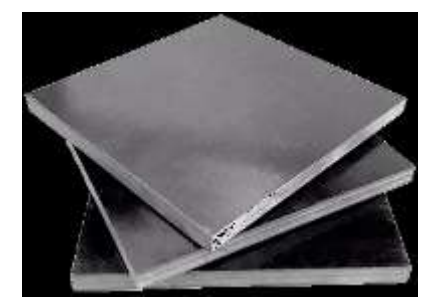


Figure 2.4: manufactured 100 mm x 100 mm CFRP plates.

#### 2.2.2. Low Velocity Impact (LVI)

Dynamic LVI tests were performed using a drop weight impact testing system equipped with a hemispherical tip following a testing procedure ASTM D7136/D7136M [21]. The impact energies on the specimens were applied by means of a drop-weight tower. The impactor mass (12.864 kg) and geometry (hemispherical tip, 10.25 mm radius) were held constant throughout the experimental program, whereas the impact energy was varied by setting the drop height appropriately. The height was determined based on the distance between the tip of the impactor head and the upper surface of the base plate. During impact specimens were held using two steel-plate fixtures, as shown in Figure 2.5. The clamping plates were fixed in place with four screws allowing the test piece to be constrained. Each set of samples was subjected to two impact energies, 40 J and 80 J.

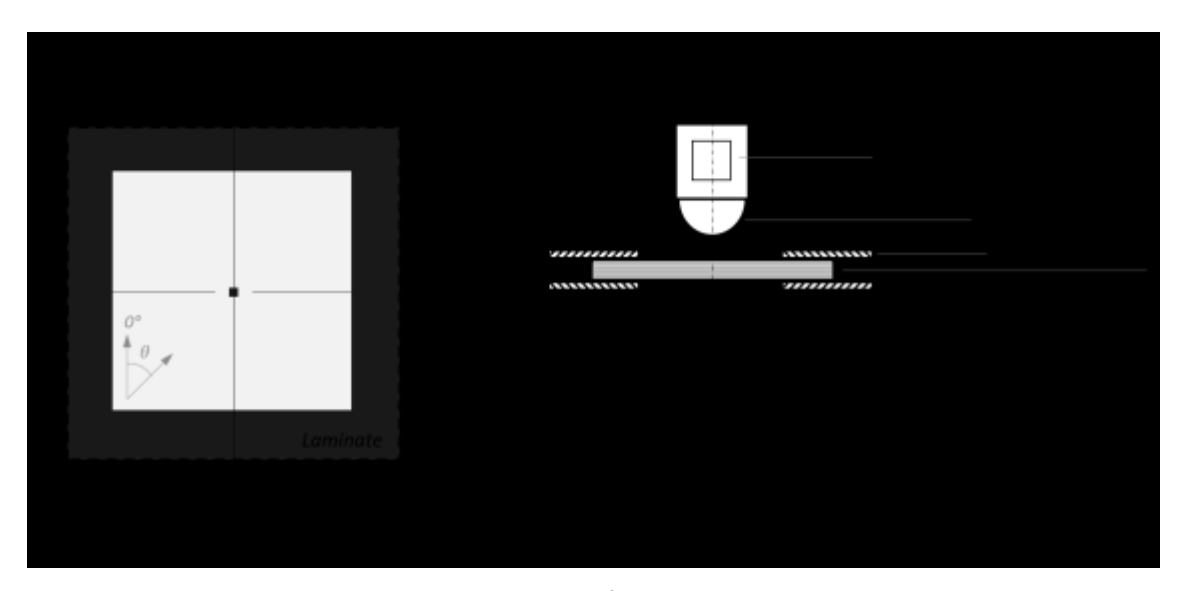


Figure 2.5: a schematic of the LVI testing setup.

During the LVI testing, the velocity of the impactor and the force exerted on it were recorded. The kinetic energy (KE) was calculated based on the velocity of the impactor, whereas the force was registered by the load cell. Using the force-time curve and assuming prefect contact between the test piece and the impactor, the displacement and the KE associated with the impactor were determined by successive integration

$$x(t) = x_0 + \left[ \int_0^t v_0 - \int_0^t \frac{F(t) - mg}{m} dt \right] dt,$$
 (7)

$$E(t) = E_0 - \frac{1}{2} m(v_0 + \int_0^t \frac{F(t) - mg}{m} dt)^2,$$
(8)

where  $x_0$  is initial (at time of first contact) displacement (assumed zero),  $v_0$  is the initial velocity (prior to impact),  $E_0$  is the initial KE (i.e. 40 J and 80 J), F(t) is the impact force and m is the mass of the impactor.

## 2.2.3. Compression After Impact (CAI)

To evaluate the residual strength of each composite laminate following the impact tests, the samples were subjected to a quasi-static compression after impact (CAI) testing by following a standard procedure ASTM D7137/D7137M [22]. Indeed, this test method is typically performed in aerospace industry to assess the ability of samples to support a load after the onset of damage. The CAI tests

were conducted using a universal testing machine (Instron, model 5585). In order to test the impacted specimens without altering their geometry, two square fixtures were used, of 100 mm x 100 mm and 200 mm x 200 mm respectively, to perform the CAI test. Figure 2.6 schematically shows the testing

setup.

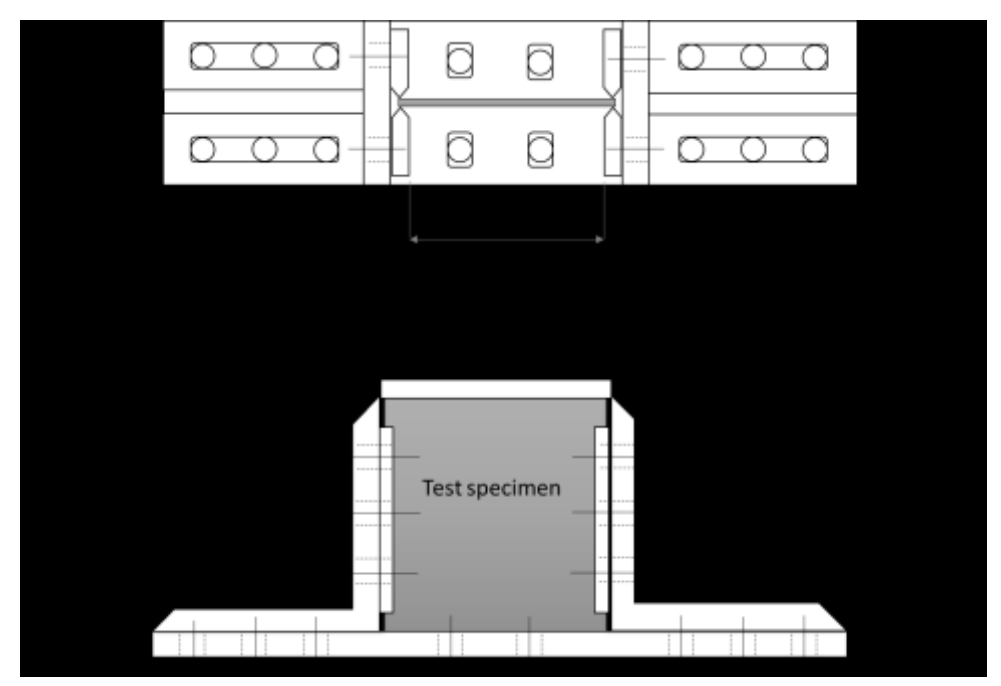


Figure 2.6: a schematic view of the CAI fixture assembly.

The fixtures stabilised the specimens at the edges without constraining the transverse deformation due to Poisson's effect. Appropriate measures were taken to ensure the flatness and parallelism when positioning and aligning the samples in the testing rig. Four strain gages along the front and back faces of the specimens were used during all tests. The recorded strain gauge data was used to determine if the specimen has been positioned in the correct way. In case the load is not applied correctly to the specimen, a bending of the sample can be detected by the strain gage data. Four samples for each configuration were end-loaded and compressed to failure. As an essential requirement for the test results to be acceptable, the compressive failure had to be confined to the impact area. In case when the samples buckled above/below the impact zone or buckled globally, the results were discarded. During CAI testing, the force, displacement and strain were recorded. Compressive residual strength can be evaluated from the peak force ( $F_{CAI}$ ) achieved during the compression of the samples divided by its cross sectional area ( $a \times h$ ), as stated in the standard test method [22]

$$\sigma_{CAI} = \frac{F_{CAI}}{a \times h}.$$
 (9)

# 3. Numerical Modelling

#### 3.1. **FEA Model**

In order to simulate a complex structural dynamic response of the composite laminates during impact events, a full 3D explicit finite element method was employed using FEA software LS-DYNA®®. A FE mesh of the computation model reproducing the experimental setup is shown in Figure 3.1. The impactor was modelled as a hemispherical elastic body with mass of 12.864 kg and a radius of 10.25 mm which is representative of the physical arrangement used in the experiments. An assumption of elastic body which does not exhibit any plastic deformation is appropriate as in the real experiments

the impact velocity was low (approx. 2.5 - 3.5 m/s) and the impactor was made of high strength steel alloy which resulted in insignificant deformation of the impactor relative to the CFRP plate. An initial velocity was applied to the nodes of the impactor to achieve the required impact energy – 40J and 80J were considered in this study.

The composite plate model was meshed using 3D solid (brick) constant stress elements with 2 elements through-the-thickness of each ply in order to capture a through-thickness stress distribution which is crucial for prediction of various failure modes including delamination. Average thickness of each ply was 0.125 mm corresponding to the total thickness of 4 mm determined from physical measurements. Constant laminate thickness with three plate sizes were considered in this analysis – 100 mm x 100 mm, 200 mm x 200 mm, 300 mm x 300 mm. A unidirectional progressive composite damage material model MAT162 of Materials Sciences Corporation [23] was assigned to each ply individually in the FE model. The use of this particular model has been successfully validated for a vast variety of low and high velocity impact events especially involving thick composites [24] structures. It considers a full 3D stress state of a finite element contrary to the assumed through-thickness stress field used by shell element formations which makes MAT162 applicable for moderately thick plates used in present analysis.

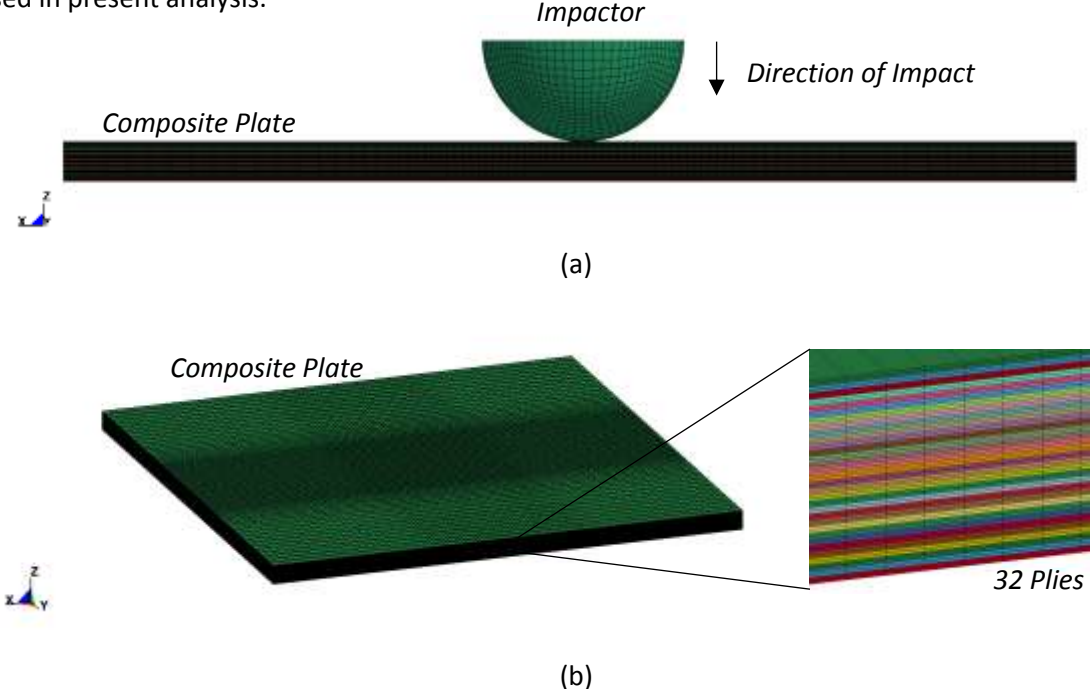


Figure 3.1: a finite element mesh used in LVI simulations with (a) a side view of the impactor and the composite target plate and (b) an isometric view of the laminate detailing the through-thickness ply definition.

The computational nodes on the top and bottom edges of the FE model of the composite plate were constrained in all translational degrees of freedom; such boundary conditions were set in order to mimic the effect of the clamps used in the impactor rig for fixing the laminates in place. All nodes relating to the impactor were constrained in X and Y direction restricting the motion to be only perpendicular to the plate. A penalty based automatic surface-to-surface contact definition was used to simulate the interaction between the impactor and the plies.

An appropriate choice of a composite material model is critical for adequate FEA simulations incorporating complex composite failure mechanisms. Therefore, further details on the chosen constitutive model are provided in the next section.

# 3.2. Progressive Composite Damage Modelling

As discussed previously, a number of techniques have been devised and used to model composite damage in general [25] and specifically in the context of helicoidal/twisted laminates [13, 15]. MAT162 used in this study is part of a standard LS-DYNA® material library and employs an orthotropic elastic behaviour until damage onset. It uses a range of progressive failure criteria developed by Hashin [26] to effectively predict initiation of fibre failure, matrix damage and delamination under various conditions such as opening, closing and sliding of failure surfaces. Composite damage progression following the failure initiation is characterised by softening behaviour based on the continuum damage mechanics (CDM) approach devised by Matzenmiller [27]. The model is capable of simulating UD as well as woven fabric composite lamina, while the UD option was selected for this study. The fibre and matrix failure criteria based on 3D stresses/strains along with a detailed description of the material model are presented in MAT162 User Manual [23]. By employing the aforementioned methodology it is possible to simulate an intrinsically complex nature of coupling between various failure modes and visualise the damage at the post-processing stage of the FEA analysis. It is important to note that even after any of the failure criteria are met, an element may still retain some residual capacity to carry loads and resist deformation in some directions. However, after accumulating significant amount of damage (as local element stiffness approaches zero,  $E \to 0$ ), an element may be required to be deleted (i.e. eroded) from the subsequent simulation as such elements no longer inhibit any residual capacity to carry loads. Therefore, in addition to the previously established failure criteria, MAT162 provides three mechanisms that enable finite element erosion or deletion from the analysis:

- 1. Fibre tensile failure is initiated and the axial tensile strain is greater than 0.015
- 2. Compressive relative volume (ratio of current volume to initial volume) in a failed element is smaller than 0.25
- 3. Expansive relative volume in a failed element is greater than 1.28

An element is deleted in case any of these conditions are met. The parameters were identified by conducting a sensitivity analysis evaluating a number of numerical simulations and comparing them to experimental results. In the post-processing, the volume of all eroded (deleted) elements was calculated and used as an indicator of the extent of the catastrophic damage incurred by the laminates. The material properties\* used in the material model MAT162 are presented in Table 3-1 and were evaluated using a combination of physical coupon testing and numerical sensitivity analysis along with extensive calibration procedures using the methodology outlined in MAT162 User Manual [23].

MID	RO (kg/m3)	EA (GPa)	EB (GPa)	EC (Gpa)	PRAB	PRCA	PRCB
162	1560	172	11.8	8.9	0.449	0.0535	0.449
GAP (GPa)	GBC (GPa)	GCA (GPa)					
4.9	4.6	2.6					
SAT (MPa)	SAC (MPa)	SBT (MPa)	SBC (MPa)	SCT (MPa)	SFC (MPa)	SFS (MPa)	SAB (MPa)
2089	1669	420	355	67	950	350	88
SBC (MPa)	SCA (MPa)	SFFC	PHIC	E_LIMIT	S_DELM		
55	76	0.3	10	0.015	1.27		
OMGMX	ECRSH	EEXPN	CRATE1	AM1			
0.99	0.25	1.28	0	2			
AM2	AM3	AM4	CRATE2	CRATE3	CRATE4		
2	0.5	0.2	0	0	0		

Table 3-1: MAT162 material model properties used in the numerical analysis.

<sup>\*</sup> RO – density; EA, EB, EC – modulus of elasticity ( $E_{11}$ ,  $E_{22}$ ,  $E_{33}$ ); PRBA, PRCA, PRCB – Poisson's ratio ( $v_{21}$ ,  $v_{31}$ ,  $v_{32}$ ); GAB, GBC, GCA – shear modulus ( $G_{12}$ ,  $G_{23}$ ,  $G_{31}$ ); SAT, SAC, SBT, SBC, SCT – normal and transverse strengths under tension and compression ( $X_1^T$ ,  $X_1^C$ ,  $X_2^T$ ,  $X_2^T$ ,  $X_2^T$ ,  $X_3^T$ ); SFC, SFS – punch crush strength & punch shear strength ( $X_3^{PCS}$ ,  $S_{13-23}^{PSS}$ ); SAB, SBC, SCA – shear strengths ( $S_{12}$ ,  $S_{23}$ ,  $S_{31}$ ). SFFC – residual compression strength factor, PHIC – coulombs friction angle in degrees, E\_LIMT –

axial strain for fibre failure, S\_DELM delamination scale factor, OMGMX – limit damage parameter, ECRSH – limit compressive volume for element erosion, EEXPN – limit expansive volume for element erosion, CERATE1-CERATE4 – strain rate parameters, AM1-AM4 – damage softening parameters.

## 4. Numerical Model Validation

## 4.1. LVI Testing

The experimental results were used to validate the devised numerical model. As explained earlier, only lamination schemes LS1, LS2 and LS4 with plate widths of 100 mm and 200 mm were considered. The general response in terms of history of kinetic energy (KE) and force vs. out-of-plane displacement for 100 mm x 100 mm plates is reported in Figure 4.1 and Figure 4.2.

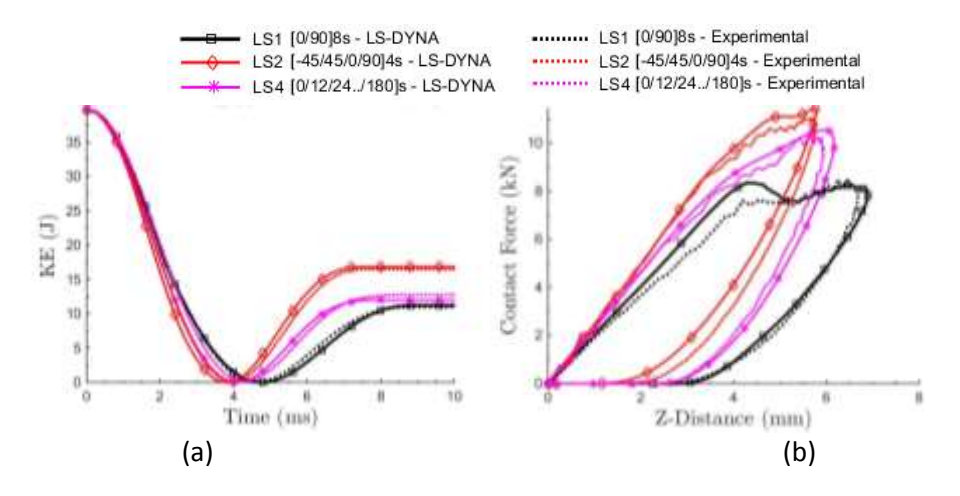


Figure 4.1: comparison between the numerical (LS-DYNA®) and experimental results for 100 mm x 100 mm plates subjected to LVI events at 40 J.

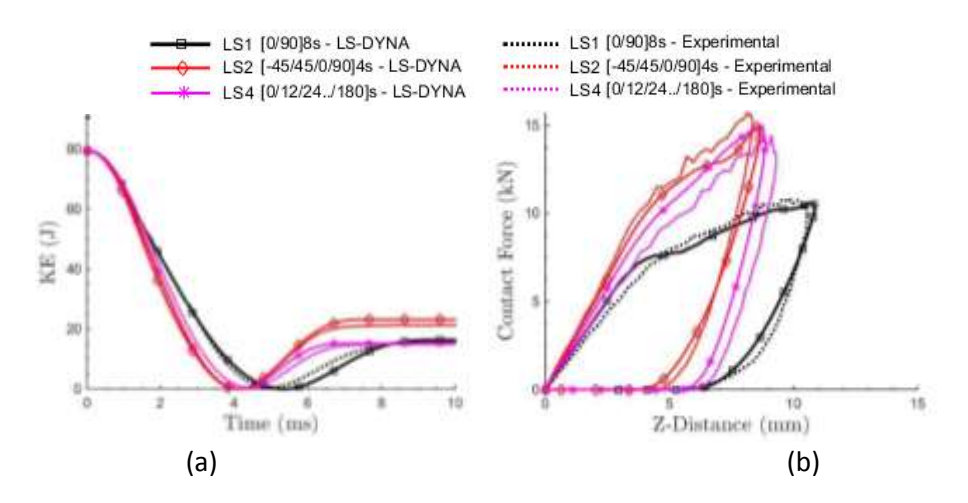


Figure 4.2: comparison between the numerical (LS-DYNA®) and experimental results for 100 mm x 100 mm plates subjected to LVI events at 80 J.

The response data shows that there was generally a very good correlation between the computational and experimental results. For clarity, the curves in Figure 4.1 and Figure 4.2 were smoothed using standard moving average filter, while the actual recorded values were used for comparing various parameters such absorbed KE (Figure 4.3) and maximum force (Figure 4.4). The absorbed energy was estimated as the difference between the initial and final KE recorded during each test.

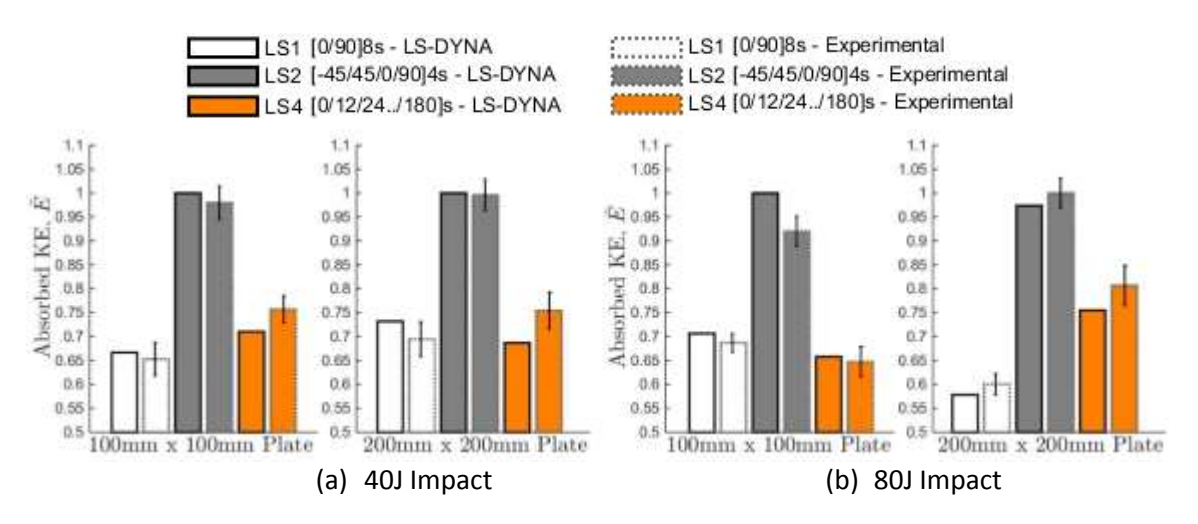


Figure 4.3: comparison between the numerical (LS-DYNA®) and experimental LVI results of the absorbed kinetic energy (normalised to the maximum value for each test configuration); error bars represent the standard deviation.

For most configurations, the experimental and numerical results correlated to within 10-15% which can be considered as a good correlation considering other results published in literature [14, 25].

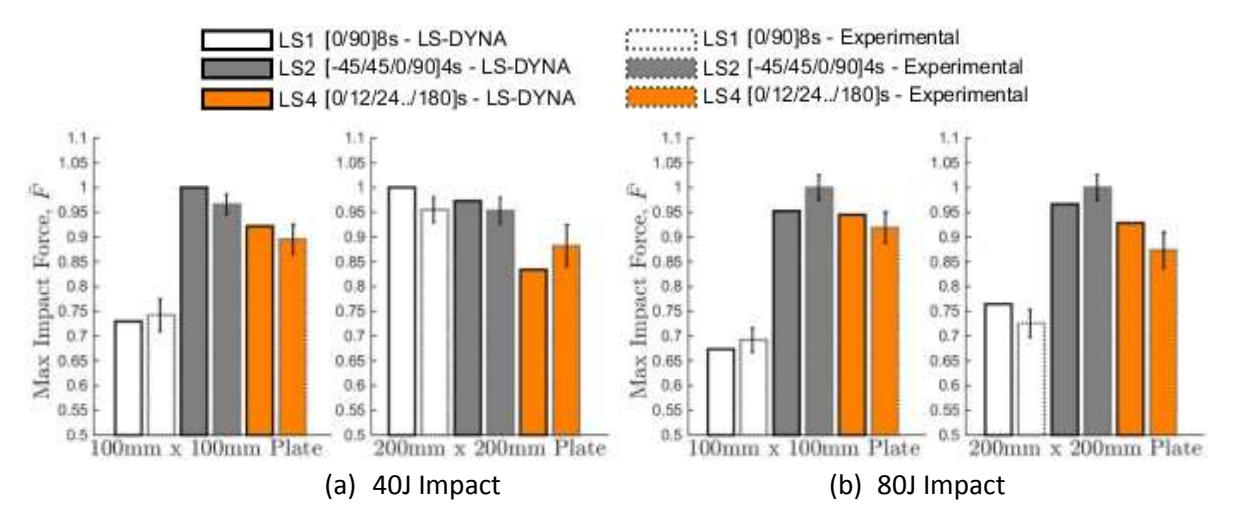


Figure 4.4: comparison between the numerical (LS-DYNA®) and experimental LVI results of the recorded peak force (normalised to the maximum value for each test configuration); error bars represent the standard deviation.

# 4.2. Damage Assessment

The composite material model MAT162 calculates the internal material damage by means of various damage criteria. However, most of these failure modes cannot be directly evaluated experimentally apart from the delamination which can be experimentally measured using a range of nondestructive testing (NDT) methods such as ultrasonic C-scan and computer tomography (CT) scanning. Moreover, delamination is by far the dangerous damage mode in laminated composite materials. Therefore, Figure 4.5 visually highlights the extent of the delamination as obtained experimentally via C-scan, and via LS-DYNA® simulations by plotting the area of finite elements that reached the damage threshold associated with the delamination.

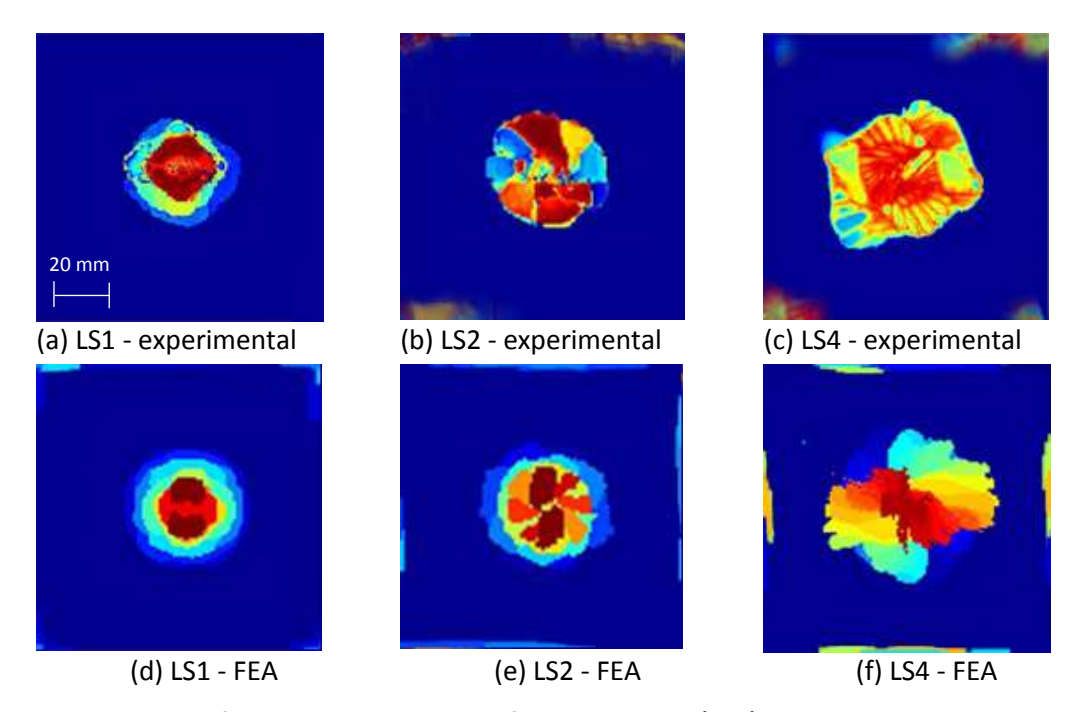


Figure 4.5: contours of the delamination extent for the impacted (40 J) 100 mm x 100 mm plates obtained using (a)-(c) ultrasonic C-scan method and (d)-(f) delamination damage mode predicted by the material model MAT162; colour shading is representative of the depth of the defect.

Evident from Figure 4.5, the delaminated area was the lowest in the cross-ply (LS1) laminates and the largest in the case of the helicoidal one (LS4). Generally, the achieved results correlated well with the experimental ones in terms of the overall area of delaminations and the shape of the delaminations. A through-the-thickness distribution of the numerically obtained delamination contours along with the comparison to the experimentally obtained CT scans of the damaged regions is shown in Figure 4.6. The dark red colour regions represent the elements that reached the delamination damage threshold, while other colours indicate the elements that are close to but have not yet failed in this failure mode. The through-the-thickness damage distribution is clearly the highest in the cross-ply (LS1) layup according to the CT scan data, whereas it is mainly arranged in-plane in the helicoidal one.

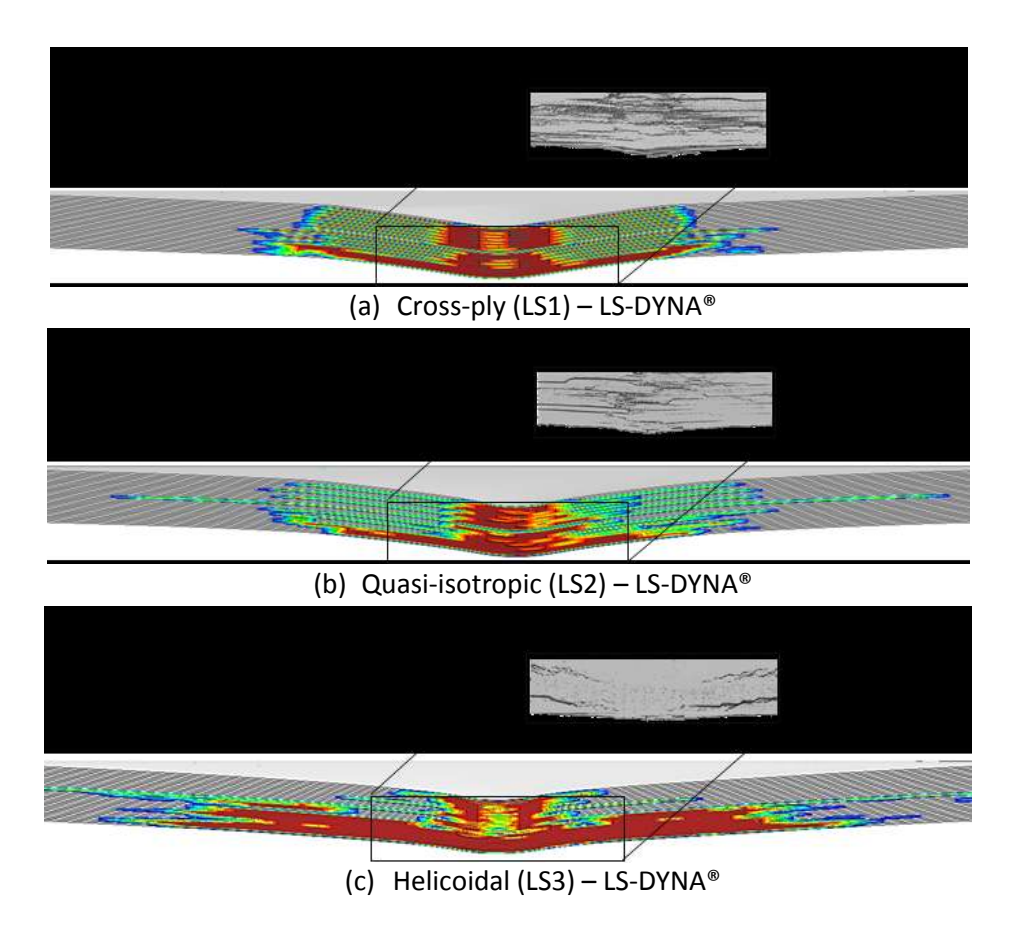


Figure 4.6: contours of delamination of 100 mm x 100 mm plate under 40J LVI event – comparison of numerical (LS-DYNA®) to experimental (CT-scan) results.

Quantitatively, a single value of delaminated area was obtained for each configuration by considering the overall extent of the delamination damage incurred by the plates in the experimental and simulated LVI test. The corresponding results are shown in Figure 4.7. A good correlation was achieved considering the published literature. Most experimental and numerical results correlated to within 10% which can be considered as a good correlation considering other results published in literature [14, 25].

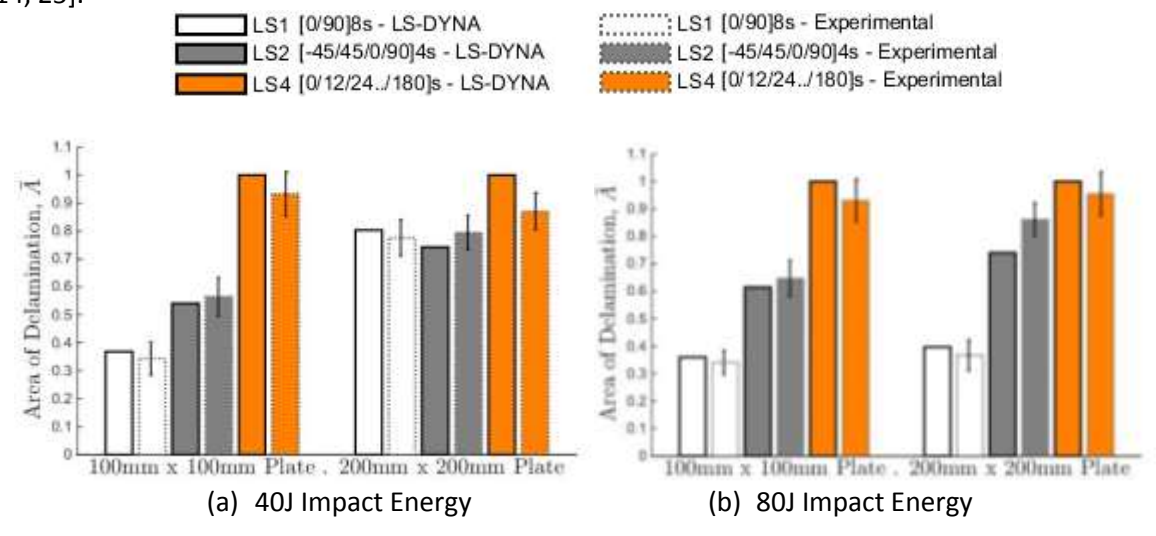


Figure 4.7: comparison between the numerical (LS-DYNA®) and experimental LVI results of the delamination area (normalised to the maximum value for each test configuration); error bars represent the standard deviation.

The damage on the back face (opposite to the impact face) was also observed and is shown in Figure 4.8. The cracks at the face are most pronounced for LS1 layup and least obvious in LS4. A virtual counterpart indicating this damage type was evident numerically as a number of finite elements were automatically eroded (deleted) from the simulation due to excessive failure and deformation driven by the internal algorithm of the material model MAT162.

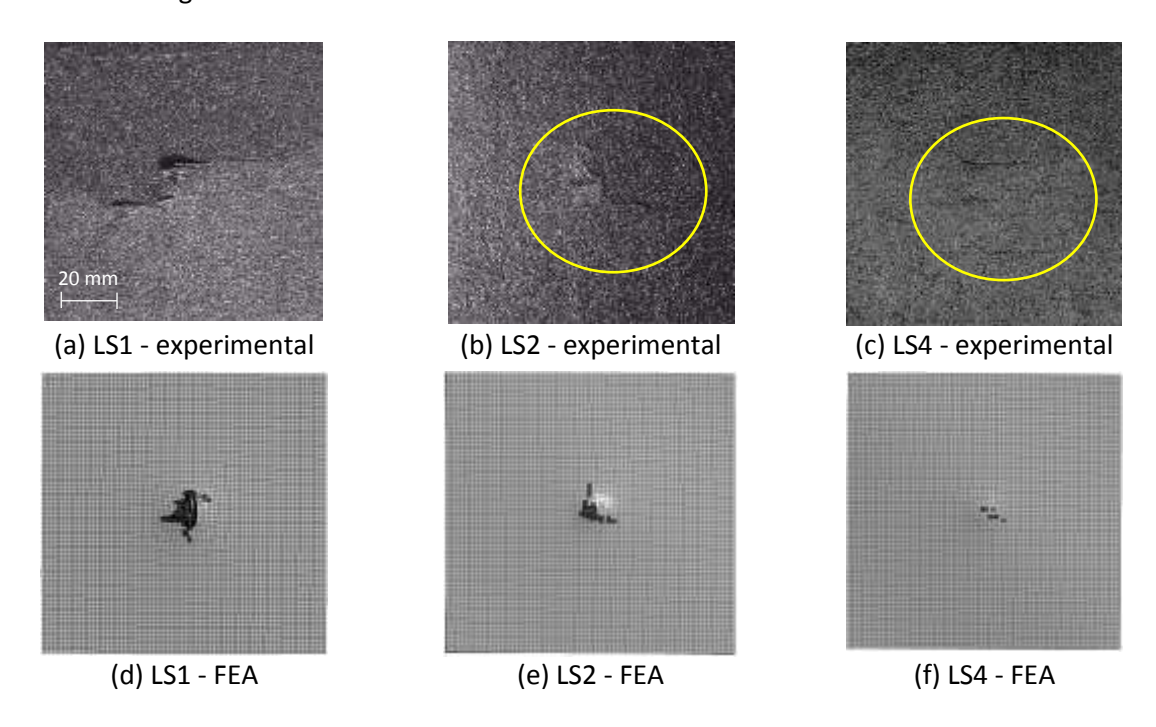


Figure 4.8: back face damage incurred by 100 mm x 100 mm plates in (a)-(c) LVI experiments; (d)-(f) LS-DYNA® simulations.

## 4.3. **CAI Testing**

Once the impact has been simulated using LS-DYNA®, the resulting model with incurred damage at the final numerical step was used for the subsequent CAI simulations. The setup used in the FEA model mimicked the experimental one and is shown in Figure 4.9. All nodes at the bottom face of the plate were constrained in all degrees of freedom, while a portion of the impact and back face of the plate were constrain in out-of-plane direction only to approximating the effect of the side guides used in the experimental setup.

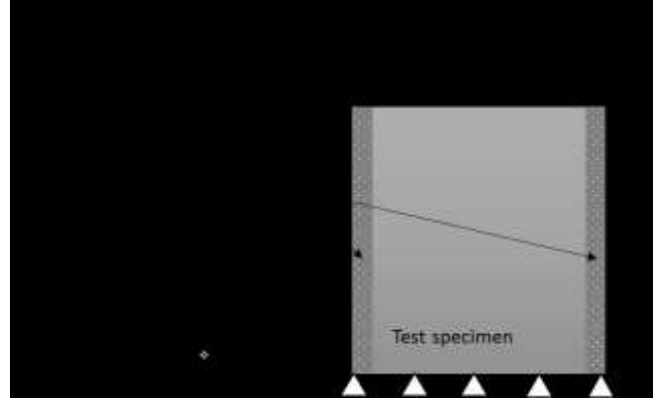


Figure 4.9: schematic view of the CAI setup used in the FEA simulations.

It is important to note that the results only for 100 mm x 100 mm plates are presented in Figure 4.10. This is due to the fact that during both numerical and experimental procedure, the larger plate sizes failed by global buckling which is according to the testing procedure invalidates the results.

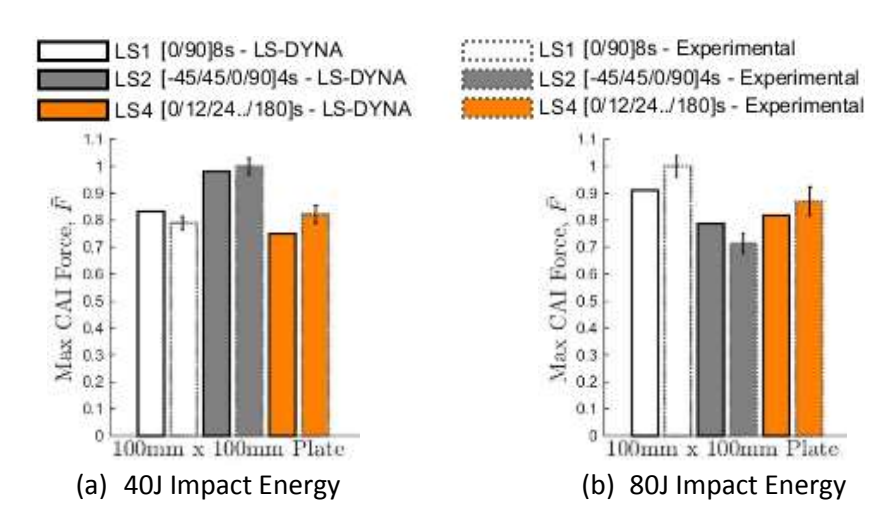


Figure 4.10: comparison between the numerical (LS-DYNA®) and experimental LVI results of the maximum recorded CAI force (normalised to the maximum value for each test configuration) for 100 mm x 100 mm plates; error bars represent the standard deviation.

Evidently from Figure 4.10, the experimental-numerical results correlated well (to with 5-10%) in terms of CAI strength as well. Quantitative results and analysis is provided in the following section.

# 5. Finite Element Analysis (FEA) Results

Following the validation procedure, the behaviour of the helicoidal samples was further evaluated by subjecting them to LVI events via numerical simulations using LS-DYNA®. The responses of the different laminates were analysed considering two impact energies (40 J and 80 J), while the energy dissipation mechanisms were also investigated by testing different samples characterised by increasing the planar dimensions, namely 100 mm x 100 mm, 200 mm x 200 mm to 300 mm x 300 mm. The results and discussion is structured in the following manner: first, the results of kinetic energy (KE), contact force and out-of-plane displacement are presented; next, the energy absorption of the various layups is analysed fixing the plate size at 100 mm x 100 mm; this is followed by the discussion of the absorbed energy and the volume of eroded element comparison considering three plate sizes at 40 J only; finally, the predicted delamination extent is presented and compared for the three plate sizes considering all layups under both 40 J and 80 J impact energies.

## 5.1. LVI Simulations

Figure 5.1, Figure 5.2 and Figure 5.3 show the results of the KE (a) evolution with time and the contact force vs. out-of-plane displacement (b) considering all five layups with various dimensions impacted at 40 J.

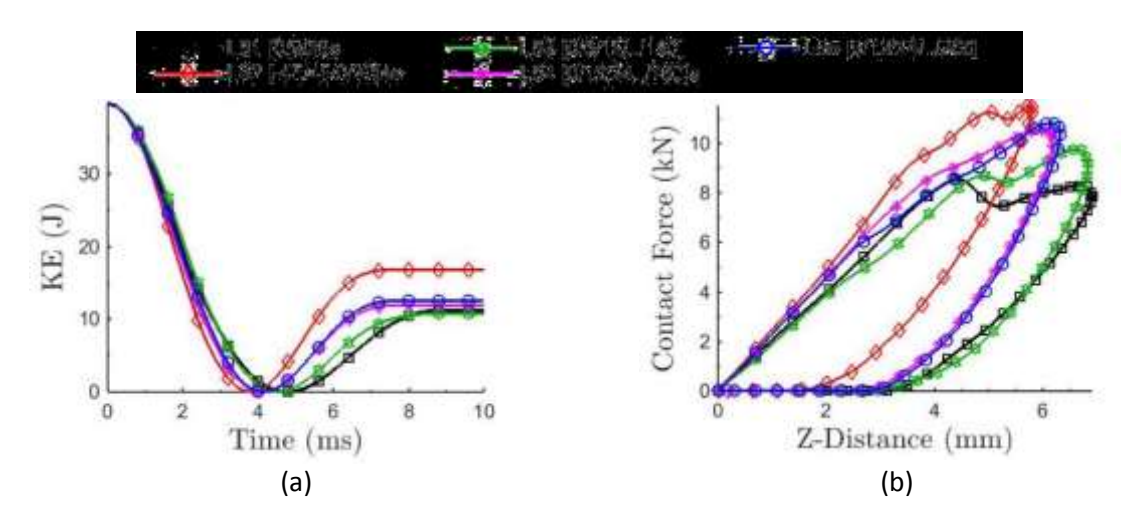


Figure 5.1: numerical results of the dynamic response of 100 mm x 100 mm CFRP plates at 40 J impact energy during LVI simulations.

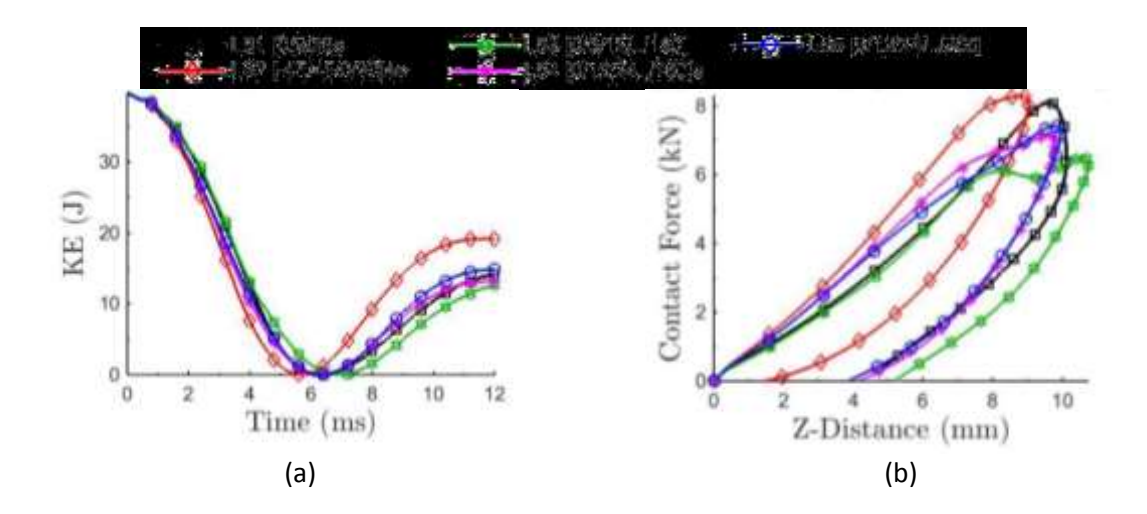


Figure 5.2: numerical results of the dynamic response of 200 mm x 200 mm CFRP plates at 40 J impact energy during LVI simulations.

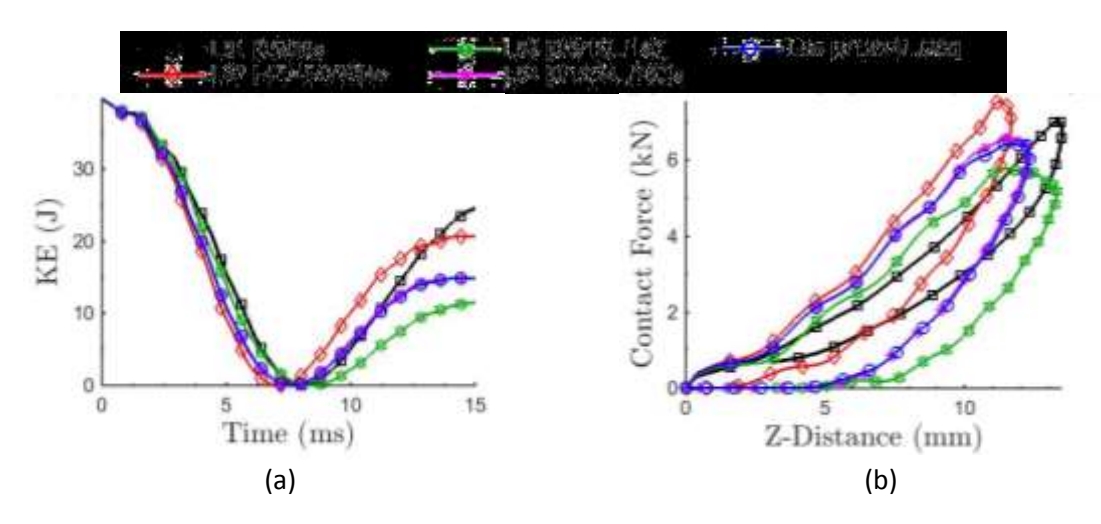


Figure 5.3: numerical results of the dynamic response of 300 mm x 300 mm CFRP plates at 40 J impact energy during LVI simulations.

As the planar size of the laminates increased, the maximum contact force and the absorbed energy decreased due to the fact that larger planar size undergoes a higher deflection while deforming more elastically. Similar trend could be observed in case of 80 J impact.

Considering only 100 mm x 100 mm plates, the results of energy absorption vs. impact energy (Figure 5.4(a)) and eroded element volume vs. impact energy (Figure 5.4(b)) are presented in respectively.

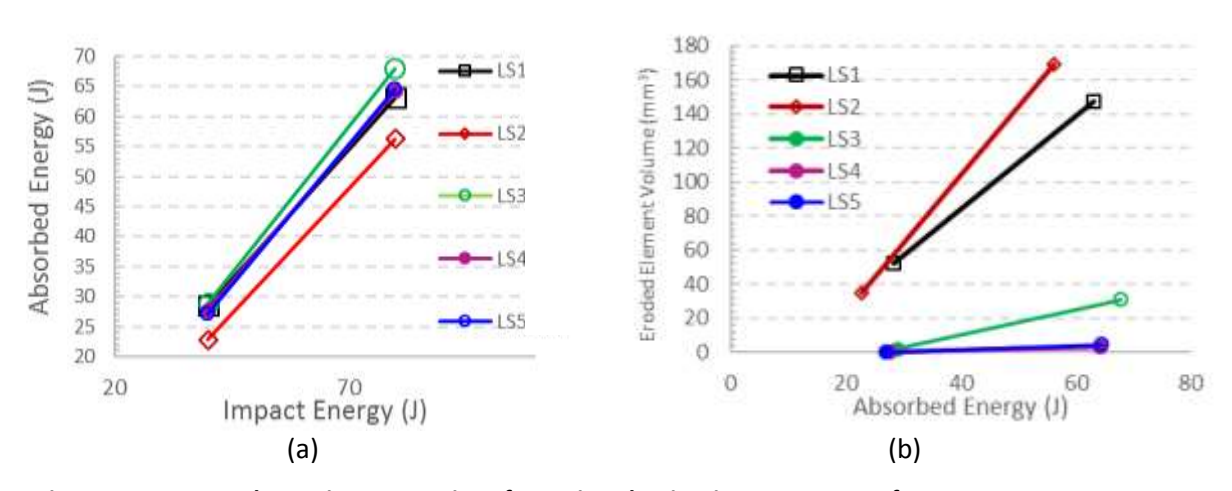


Figure 5.4: energy absorption comparison for various lamination sequences of 100 mm x 100 mm CFRP plates.

As it is possible to see in Figure 5.4(a), for the 40 J impact, all the helicoidal arrangements (LS3, LS4 and LS5) overcome the quasi-isotropic layup (LS2), showing an enhancement in the energy absorption by more than 26.6%. The highest energy absorption value belongs to the helicoidal arrangement LS3 (6° pitch angle), while increasing the pitch angle up to 12 degrees leads to a decrement in the value of absorbed energy by almost 5% (from 28.96 J to 27.75 J), which is consistent with the data present in literature. However, in this case, the difference between the asymmetric (LS5) and symmetric layup

(LS4) is almost negligible (~2%). Indeed, in practical terms, several percent difference is not significant; although the results presented in this section are numerical and therefore would yield the same values if repeated, the validation study showed that experimentally there can be a variability of about 5-10% due to variabilities in the manufacturing and testing of the samples.

The different behaviour of the laminates in bending can be explained by analysing the mismatch between two consecutive layers in the different arrangements. Bending modulus is a key characteristic in the interlaminar strength of a laminate especially for mode-II (in-plane shear). Considering two unidirectional layers placed at 0°, the high bending modulus of the resulting laminate means that more energy can be dissipated via opening of the fracture surface at the interphase (i.e. delamination). Since the mismatch between two following laminae decreases moving between crossply (LS1, 90°), quasi-isotropic (LS2, 45°), helical (LS4 and LS5, 12°) and helical (LS3, 6°), the resulting bending modulus of the laminate increases leading to a higher energy absorption capability for the helicoidal laminates [28].

The cross-ply lamination sequence (LS1) displayed interesting behaviour as it preformed second best after LS3 in terms of energy absorption, absorbing only 0.47 J (~2.5%) less than the best helicoidal sample with 6° pitch angle (LS3). This seems to be in contrast with previous results obtained in literature that show an increase in the impact resistance for lower pitch angles [13, 29, 30] in comparison with traditional cross-ply laminates. This behaviour can be explained by taking into account the internal damage distribution for the different laminates as represented in Figure 4.6 and Figure 5.4(b). As it is possible to see, both cross-ply (LS1) and quasi-isotropic (LS2) layups show a higher through-the-thickness damage distribution and indeed higher volume of eroded elements, while all the helicoidal samples appear completely undamaged after the impact. Indeed, due to the small angle between two subsequent layers, the helicoidal sequence is able to absorb the impact by distributing its energy all over the sample elastically with minimal internal damage, while traditional laminates dissipate impact energy predominantly via the creation of new surfaces (delaminations and internal cracks). This mechanism absorbs enough energy to bring the total energy absorption of the cross-ply laminate up to the value comparable with the helicoidal samples. It is important to underline that although the levels of absorbed energy are similar for both the cross-ply and the helicoidal samples, the former one results in more critically damaged samples indicated by the volume of eroded elements (Figure 5.4(b)).

The beneficial effect of the helicoidal arrangement is clearer when the same lamination sequences are impacted at higher energy levels (80 J) as represented in Figure 5.4(b). As it is possible to see from the curves, in this case the helicoidal arrangement in LS3, LS4 and LS5 allows a better distribution of the energy during the impact event, resulting in an increased value of the absorbed energy in comparison with the LS1 and LS2. Analysing the eroded element volumes for these laminates, it is possible to note that for 80 J, the discrepancy between traditional and helical layup is more pronounced: the traditional layup sequences still require the opening of new surfaces to absorb the impact energy, however, this mechanism was not sufficient to reach the absorbed energy displayed by the helicoidal arrangements. Further considering the helical arrangements, it is possible to notice that the pitch angle plays a key role in the enhancement of the interlaminar toughness. Moving from 12° (LS4 and LS5) to 6° (LS3) it is possible to observe an enhancement in the energy absorption of 5%. It is important to note that in the case of the helicoidal arrangements, a smaller amount of internal damage (volume of eroded elements) was recorded compared the traditional layups (-81%). However, it is also essential to note that the delamination extent was higher in case of helicoidal laminates as shown in Figure 4.5. Therefore, there is a clear difference in the prevailing failure mechanisms which are characteristic to standard and helicoidal composites.

When a sample is subjected to a low velocity impact, the contact between the penetrator and the sample is long enough for the entire structure to respond to the impact, therefore the dynamic structural response is strongly affected by the dimensions of the specimen. Based on this premise, the effect of the sample dimensions was investigated by testing samples at 40 J with different dimensions, 100 mm x 100 mm, 200 mm x 200 mm and 300 mm x 300 mm.

The performance of all the lamination sequences considering various plate sizes in presented in Figure 5.5.

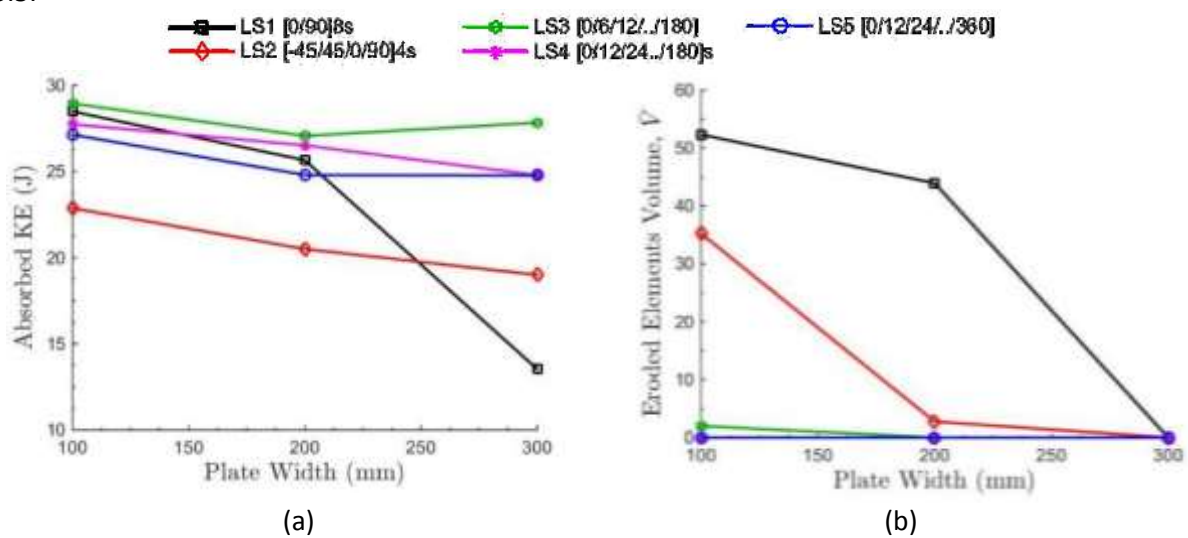


Figure 5.5: absorbed energy and volume of eroded elements for various CFRP plate sizes subjected to impact energy of 40 J.

Evident from Figure 5.5, when a larger plate size is used, the results show a general decrease of the energy absorption for all the samples as a larger structural area is available for the elastic response of the entire specimen. Analysing the results further, the energy absorption corresponding to the crossply and quasi-isotropic laminate (LS1) drops down losing more than 50% (from 28.49 J to 13.53 J) and almost 20% (from 22.87 to 19.00J) respectively, the helicoidal arrangements lose merely an average of 8%. The large drop in the value of absorbed energy for the cross-ply layup sequence can be explained by analysing how the increase in the sample dimensions influence the volume of eroded elements for the different laminates. Examining Figure 5.5(b), it appears clear that the cross-ply laminate is the layup that is most affected by the dimensional change since the volume of eroded elements drops down from 52.33 to 0 mm<sup>3</sup>. As we observed previously, because of the large mismatch between two subsequent layers the only way the cross-ply arrangement has to dissipate energy is by opening new surfaces, hence creating intra and inter layer damages. Since the increase of the dimensions of the sample allows the entire surface to respond to the external excitation more elastically, this mechanism (the formation of new surfaces) is suppressed. On the other hand, since the helicoidal arrangement provides a good elastic dissipation of energy without the need of large fracture areas, the change in the dimensions of the samples leads to a marginal difference in the response of LS3, LS4 and LS5. Further considering the helicoidal arrangements, there is an inverse proportion between the pitch angle of the helical layup and impact resistance when larger dimensions are used: for both 200 mm x 200 mm and 300 mm x 300 mm samples, the sample with 6° (LS3) pitch displays higher values of absorbed energy in comparison with the one with 12° (LS5), showing an increase of 9% and 12% respectively. Moreover, it is important to note that the symmetry of the lamination sequence affects the energy absorption mechanism when different dimensions are used.

Indeed, it appears that the asymmetric lamination of LS3 and LS5 leads to a nonlinear variation in the absorbed energy with the changing sample dimensions, showing first a decrease in the passage between 100 mm x 100 mm and 200 x 200 mm of 6.5% and then an increase of 3% when the dimensions are further increased up to 300 mm x 300 mm. For comparison, the symmetric layup sequence of LS2 and LS3 leads to a more traditional linear behaviour.

In addition to the volume of eroded elements, the composite material model MAT162 calculates the extent of delamination among other damage modes. Figure 5.6 presents the results of overall delamination for increasing plate widths for simulated LVI events under the impact energies of 40 J and 80 J; this was calculated by summing the area of finite elements for all layers that reached the damage threshold associated with the delamination failure mode

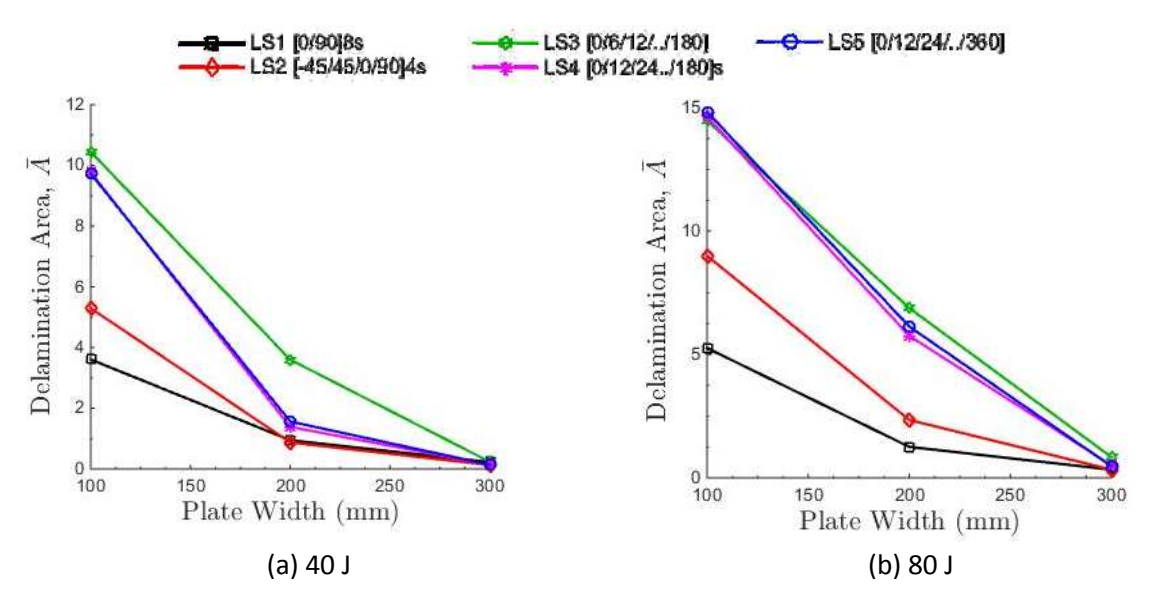


Figure 5.6: total delamination area (normalised according to the plate area) vs. plate width under LVI impact energy of (a) 40 J and (b) 80 J.

As can be seen from Figure 5.6, the delamination areas decreased with increasing plate width which allowed the structure to distribute the impact energy across a larger area enabling higher degree of elastic deformation. Notably, the cross-ply (LS1) laminates displayed the least amount of delamination as most of the energy was absorbed through open fracture indicated by the high number of eroded elements which is ultimately symptomatic of catastrophic failure. Although, the area of delamination for helicoidal laminates was consistently estimated as higher than for cross-ply and quasi-isotropic ones, helical configurations especially LS4 and LS5 showed a significant improvement as the plate size was increased. For instance, at 40 J the overall delamination area calculated for LS4 and LS5 was almost twice the one obtained for quasi-isotropic (LS2) laminates with plate size of 100 mm x 100 mm with, while the difference subsequently reduced to about 65% using 200 mm x 200 mm plates. Similar but less pronounced trend was observed at 80 J considering a transition from 100 mm x 100 mm to 200 mm x 200 mm plates as at higher energy the impact response becomes more localised to the area of incipient striker contact and the structure has less time to respond globally. However, as the plate size increased from 200 mm x 200 mm to 300 mm x 300 mm under impact energy of 80 J, the helicoidal laminates improved to a larger extent than the quasi-isotropic one, although, the overall delaminated area was still higher. Evidently, the helicoidal layups are absorbing energy more efficiently (i.e. with less damage) as the plate size increases. It is also important to note that while there was a good correlation between the experimentally obtained (C-scan) delamination areas and the numerically estimated one, the CT-scan showed a higher distribution of damage through-the-thickness of the cross-ply and quasi-isotropic plates than in the case of helicoidal ones.

Moreover, it is possible to plot the contours of finite elements that failed in longitudinal fibre mode as predicted by the material model MAT162. It is also important to note that no NDT technique currently exists that can evaluate the internal damage in such a way that enables to reliably discern between the longitudinal fibre damage (in tension/compression) and other failure modes, whereas this becomes possible by employing a FEA modelling approach using LS-DYNA® with material mode MAT162.

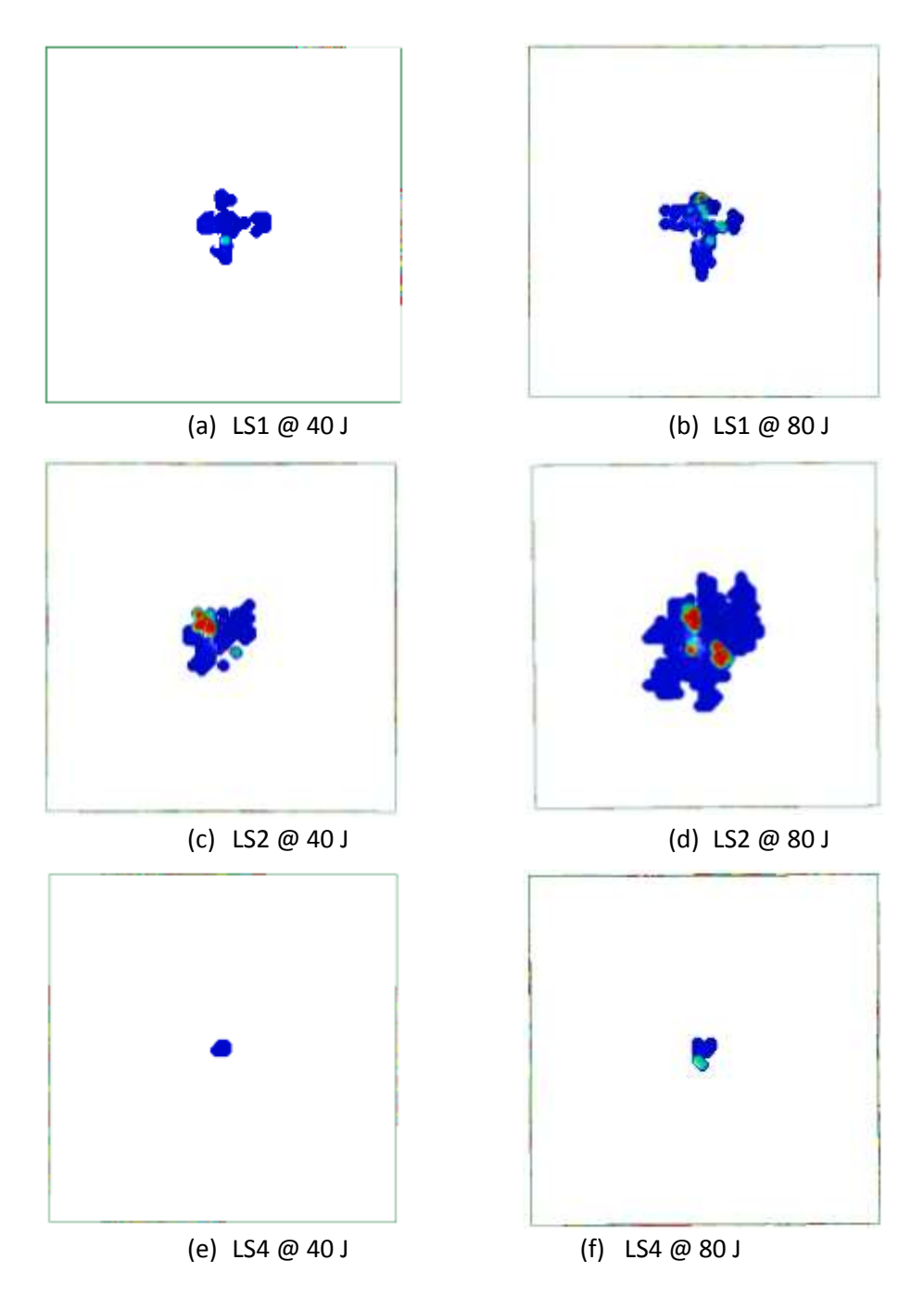


Figure 5.7: contours of iso-surfaces of the finite elements (after LVI but prior to CAI testing) that failed in longitudinal fibre mode as predicted by MAT162; plates size 100 mm x 100 mm.

The importance of the extent of fibre failure is particularly important in the case of CAI testing which is further addressed in the following section.

#### 5.2. **CAI Simulations**

Following the analysis of impact damage induced during simulated LVI events, simulations of compression after impact (CAI) were performed. In this procedure, the finite element mesh along with the incurred damage and the material properties at the last simulation step of the LVI cases were used as an input to CAI simulations, whereby the samples were end-loaded and compressed to failure. All tests were carried out in a manner that avoids global buckling of the impacted specimens; only 100 mm x 100 mm plates were used in CAI simulations as higher plate dimensions tended to buckle globally which invalidates the CAI tests. CAI strength is one of the most critical properties from a design/structural point of view. The CAI simulations give the ability of the sample to carry load following the onset of damage. Indeed, the test is sometimes used as an index of the toughness of the sample. Compressive residual strength was evaluated from the peak force ( $F_{CAI}$ ) attaiend during the compression of the samples divided by its cross sectional area ( $a \times h$ ), as specified in the standard procedure [22]. The details of the residual strength are presented in Figure 5.8 with the percentage change, using the quasi-isotropic (LS2) CAI strength as a reference (control) sample.

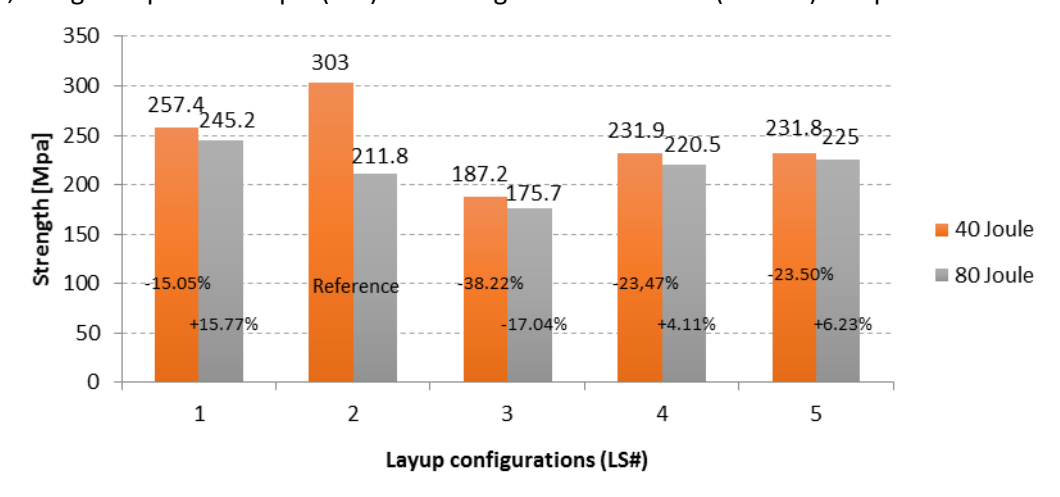


Figure 5.8: CAI strength obtained from the LS-DYNA® simulations using post-impacted 100 mm x 100 mm plates.

At both 40 J and 80 J, the configuration LS3 (6°) with the smallest angle used for the helicoidal layup shows the lowest CAI strength. Instead, the helicoidal layups LS4 (12°) and LS5 (12°) show a small increase (  $\sim$ 4% and  $\sim$ 6% percent respectively) in residual strength with respect to the quasi-isotropic configuration. Furthermore, considering the layups with their corresponding rotational angle, the obtained CAI strength trends are consistent with the ones published by Grunenfelder et al. [15], although, they used a different composite material and impact energy.

In order to understand the reasons behind the difference in results at 40 J and 80 J, it is important to consider the longitudinal fibre damage mode as during the CAI testing the load is resisted primarily by the fibres. At impact energy of 40 J, the cross-ply (LS1) and quasi-isotropic layups (LS2) outperformed the helicoidal ones as at this impact energy level, the fibre-related stiffness degradation experienced by LS1 and LS2 was not sufficient to reduce the CAI strength below the values recorded for the helicoidal laminates. Indeed, considering a very small impact energy or indeed in a damage-free state, lamination sequences LS1 and LS2 are expected to withstand higher loads before failure than helicoidal ones as LS1 and LS2 contain more layers with fibres oriented in the direction of applied loading. However, at higher energy, more fibre damage is incurred by the quasi-isotropic (LS2) laminate as the helicoidal ones are more effective at distributing the damage in-plane resulting in less fibre fracture prior to CAI testing. This in not just a hypothetical explanation. This was confirmed by plotting the contours of finite elements that failed in longitudinal fibre mode prior to CAI testing as predicted by the material model MAT162. Furthermore, in the case of the cross-ply (LS1) composite

plate, the fibre damage is more localised to the incipient impact location and therefore it experienced the least reduction in CAI strength at the higher impact energy.

#### 6. Conclusions

In this work, the impact resistance of CFRP laminates with plies arranged in various bio-inspired helicoidal layups was evaluated. Full 3D FEA simulations of the LVI and CAI testing were performed using LS-DYNA® with an advanced composite constitutive model MAT162. In comparison to the crossply and quasi-isotropic controls, the helicoidal laminates exhibited a lower degree of internal damage through the thickness of the plates which was confirmed experimentally by the CT scans and numerically by plotting the volume of eroded elements and the contours of finite elements failed in longitudinal fibre mode. However, higher delaminations extent was recorded for the helicoidal layups compared to the controls which is consistent with the published research. Three plate sizes were considered and it was found that the helicoidal laminates tend to dissipate the impact energy more efficiently by spreading it in-plane and with less damage as the plate size is increased, assuming all other parameters are kept the same. This was especially true for the smaller impact energy given that as the velocity and the impact energy is increased, the dynamic response of the specimens becomes more localised. Interestingly, some nonlinear relation between the absorbed energy and the plate size was recorded for the bio-inspired lamination sequences. CAI testing revealed that at a higher energy, the residual strength of these laminates was higher than for the aerospace standard quasi-isotropic one. Although, only the smallest plate size was used for the CAI testing due to the onset of global buckling for the larger plate sizes.

It is worth noting that while research evidence in support of Bouligand stacking configurations was shown, there is not yet clear indication that any composite utilising industry is using or seriously considering the use of such layups for real world applications. This is partly due to the manufacturing complexity involved in using the non-standard inter-ply angles but also due to the lack of research knowledge associated with performance of twisted composite architectures. Therefore, it is envisioned that the outcome of this research will lead to further studies and pave the way for the helicoidal laminates being used, in combination with their classical counterparts, for example, in aircraft radome, fuselage, leading edge protection and other applications requiring damage tolerance.

# 7. Acknowledgement

The work presented herein has been performed as part of ALAMSA project supported and funded by the European Union (EU) in the 7<sup>th</sup> framework programme (FP7) for research and technological development.

## 8. References

- 1. Wegst, U.G.K. and M.F. Ashby, *The mechanical efficiency of natural materials*. Philosophical Magazine, 2004. **84**(21): p. 2167-2186.
- 2. Wegst, U.G.K., et al., Bioinspired structural materials. Nat Mater, 2015. 14(1): p. 23-36.
- 3. Yang, W., et al., Flexible Dermal Armor in Nature. Jom, 2012. **64**(4): p. 475-485.
- 4. Yang, W., et al., *Natural flexible dermal armor*. Adv Mater, 2013. **25**(1): p. 31-48.
- 5. Luz, G.M. and J.F. Mano, *Biomimetic design of materials and biomaterials inspired by the structure of nacre*. Philos Trans A Math Phys Eng Sci, 2009. **367**(1893): p. 1587-605.
- 6. Bouligand, Y., *Twisted fibrous arrangements in biological materials and cholesteric mesophases.* Tissue and Cell, 1972. **4**(2): p. 189-217.
- 7. Patek, S.N. and R.L. Caldwell, Extreme impact and cavitation forces of a biological hammer: strike forces of the peacock mantis shrimp Odontodactylus scyllarus. J Exp Biol, 2005. **208**(Pt 19): p. 3655-64.
- 8. Weaver, J.C., et al., *The stomatopod dactyl club: a formidable damage-tolerant biological hammer.* Science, 2012. **336**(6086): p. 1275-80.
- 9. Milliron, G., Lightweight Impact-Resistant Composite Materials: Lessons from Mantis Shrimp. 2012.
- 10. Giraud, M.M., et al., *The fibrous structure of coelacanth scales: A twisted 'Plywood'*. Tissue and Cell, 1978. **10**(4): p. 671-686.
- 11. Giraud-Guille, M.-M., *Twisted plywood architecture of collagen fibrils in human compact bone osteons*. Calcified tissue international, 1988. **42**(3): p. 167-180.
- 12. Chen, B., et al., *Helicoidal microstructure of Scarabaei cuticle and biomimetic research.* Materials Science and Engineering: A, 2006. **423**(1-2): p. 237-242.
- 13. Apichattrabrut, T. and K. Ravi-Chandar, *Helicoidal Composites*. Mechanics of Advanced Materials and Structures, 2006. **13**(1): p. 61-76.
- 14. Cheng, L., et al., *Mechanical behavior of bio-inspired laminated composites*. Composites Part A: Applied Science and Manufacturing, 2011. **42**(2): p. 211-220.
- 15. Grunenfelder, L.K., et al., *Bio-inspired impact-resistant composites*. Acta Biomater, 2014. **10**(9): p. 3997-4008.
- 16. Ngern, N.H., J.S. Shang, and V.B. Tan, *Impact Performance Of Biomimetic Helicoidal Composite Plates*. 2015.
- 17. Andersons, J. and M. König, *Dependence of fracture toughness of composite laminates on interface ply orientations and delamination growth direction*. Composites Science and Technology, 2004. **64**(13-14): p. 2139-2152.
- 18. Reddy, J.N. and J.N. Reddy, *Mechanics of laminated composite plates and shells : theory and analysis.* 2nd ed. 2004, Boca Raton, FL; London: CRC Press. xxiii, 831 p.
- 19. Sánchez-Sáez, S., et al., *Compression after impact of thin composite laminates.* Composites Science and Technology, 2005. **65**(13): p. 1911-1919.
- 20. Duarte, A., I. Herszberg, and R. Paton, *Impact resistance and tolerance of interleaved tape laminates*. Composite structures, 1999. **47**(1): p. 753-758.
- 21. ASTM D7136 / D7136M-15, Test Method for Measuring the Damage Resistance of a Fiber-Reinforced Polymer Matrix Composite to a Drop-Weight Impact Event. 2015, ASTM International: www.astm.org.
- 22. ASTM D7137 / D7137M Test Method for Compressive Residual Strength Properties of Damaged Polymer Matrix Composite Plates. 2012, ASTM International.
- 23. Gama, D.B.Z., A Progressive Composite damage Model for Undirectional and Woven Fabric Composites, MAT162 Composite DMG MSC. 2014, Materials Sciences Corporation & University of Delaware Center for Composite Materials.
- 24. Gama, B.A. and J.W. Gillespie, *Finite element modeling of impact, damage evolution and penetration of thick-section composites.* International Journal of Impact Engineering, 2011. **38**(4): p. 181-197.

- 25. Heimbs, S., et al., Low velocity impact on CFRP plates with compressive preload: Test and modelling. International Journal of Impact Engineering, 2009. **36**(10-11): p. 1182-1193.
- 26. Hashin, Z., *Failure criteria for unidirectional fiber composites*. Journal of applied mechanics, 1980. **47**(2): p. 329-334.
- 27. Matzenmiller, A., J. Lubliner, and R. Taylor, *A constitutive model for anisotropic damage in fiber-composites.* Mechanics of materials, 1995. **20**(2): p. 125-152.
- 28. Kim, B.W. and A.H. Mayer, *Influence of fiber direction and mixed-mode ratio on delamination fracture toughness of carbon/epoxy laminates*. Composites Science and Technology, 2003. **63**(5): p. 695-713.
- 29. Li, V.C., Y. Wang, and S. Backer, *Effect of inclining angle, bundling and surface treatment on synthetic fibre pull-out from a cement matrix.* Composites, 1990. **21**(2): p. 132-140.
- 30. Tao, J. and C. Sun, *Influence of ply orientation on delamination in composite laminates*. Journal of Composite Materials, 1998. **32**(21): p. 1933-1947.